INVESTIGATION OF ELECTRO-OPTICAL TECHNIQUES FOR CONTROLLING THE DIRECTION OF A LASER BEAM

Interim Report

Contract NAS 8-11459

(Continuation of NASw-731)

March 29, 1965

National Aeronautics and Space Administration
George C. Marshall Space Flight Center
Huntsville, Alabama

GENERAL TELEPHONE & ELECTRONICS LABORATORIES
INCORPORATED

BAYSIDE LABORATORIES, BAYSIDE, NEW YORK

TR 65-722.8

INVESTIGATION OF ELECTRO-OPTICAL TECHNIQUES FOR CONTROLLING THE DIRECTION OF A LASER BEAM

INTERIM REPORT

Contract NAS 8-11459
(Continuation of NASw-731)

PART ONE - BEAM DEFLECTOR DEVICES

V.J. Fowler
J. Schlafer

PART TWO - BEAM DEFLECTOR SYSTEMS

S. Kapuscienski
R. Johnson
P. Weiss

March 29, 1965

ABSTRACT

An investigation of a system for optical acquisition and tracking is described. Part I of the report is concerned with the experimental development of the key component of the system, a laser beam steerer which uses piezoelectrically driven mirrors. Consideration is given to maximum attainable resolution, frequency response, hysteresis, thermal and aging effects, and unwanted modes of deflection. Part II deals mainly with the theoretical aspects of the system. This section discusses types of scan modes, range calculations, and noise analysis including combined effects of atmospheric and shot noise. Also described are results of a one dimensional tracking system incorporating shear plate deflectors.

PREFACE

The work being reported here is a continuation of research previously reported in the Final Report on Contract NASw-731, "Investigation of Electro-Optic Techniques for Controlling the Direction of a Laser Beam," issued 10 August 1964 by the General Telephone & Electronics Laboratories, Bayside, New York. That previous program included the design, development, and evaluation of a number of electro-optic variable refraction deflectors and piezoelectric shear-plate mirror deflectors. All of these structures have inherent capabilities for extremely rapid deflection, although high-speed operation was not an objective of that program. It was concluded that precision deflection is feasible but difficult, requiring temperature stabilization and high field correction.

The objectives of the present program were:

1. To develop and evaluate a bench test model of a one-dimensional beam deflection and tracking and acquisition system, using deflectors developed in the previous program.

2. To design an experimental model of an open-loop acquisition system using a two-dimensional high-speed deflector.

3. To establish physical limitations for achieving high-precision deflection for acquisition and tracking applications.

4. To establish design, fabrication, and test procedures for high-speed precision deflectors.

5. To develop block diagrams for subsystems for sensing beam direction errors and for processing error signals as required for typical applications.

6. To determine the effects of modulation and noise on the precision of acquisition and tracking.

Part I of this report covers work on the theoretical and experimental investigation of the deflector devices, performed at General Telephone & Electronics Laboratories, Bayside, New York by V. Fowler and J. Schlafer. Part II covers work on the theoretical and experimental investigation of optical acquisition systems using beam deflectors, performed at Sylvania Electronic Systems, Central, Williamsville, New York by S. Kapuscienski, R. Johnson, and P. Weiss.

TABLE OF CONTENTS

		Page
	Abstract	iii
	Preface	v
	PART I - BEAM DEFLECTOR DEVICES	
1.	INTRODUCTION	1
2.	CHOICE OF DEVELOPMENTAL MODEL	2
	2.1 Theoretical Resolution Limitations	2
	2.2 Comparison of Other Characteristics	5
3.	CHARACTERISTICS OF EXPERIMENTAL DEFLECTORS	6
	3.1 Hysteresis	6
	3.1.1 Effect of Hysteresis on Precision of Deflection	6
	3.1.2 Polarization Measurement of Deflection	7
	3.2 Resonance Effects	8
	3.2.1 Pulsed Operation	8
	3.2.2 Structural Acoustic Resonance	8
	3.3 Temperature and Aging Effects	12
	3.3.1 Precision Deflection Measurements	12
	3.3.2 Temperature-Induced Drift	14
	3.3.3 Temperature Dependence of Deflection Versus Polarization	16
	3.3.4 Aging	16
4.	DEVELOPMENT OF NEW DEFLECTORS	16
	4.1 Symmetrically Supported Mirror Deflector	16
	4.2 Ruggedized Shear Plate Model	17
	4.2.1 The Unit Cell	18
	4.2.2 Balancing of Thermally Induced Motion	19
	4.2.3 Construction Techniques	20
	4.2.4 Experimental Results	20
5.	CONCLUSIONS	21

TABLE OF CONTENTS (Continued)

	Page
PART II - BEAM DEFLECTOR SYSTEMS	
1. INTRODUCTION	23
2. SYSTEM ANALYSIS	24
2.1 Beam Deflectors as System Components	24
2.2 Scan Modes	24
2.2.1 Sawtooth Scan	24
2.2.2 Triangular Scan	25
2.2.3 Sinusoidal Scan	26
2.2.4 Spiral Scan	26
2.3 System to Acquire and Track a Corner Reflector	28
2.3.1 Bradley or Transit Time Error	30
2.4 Range Calculations	30
2.5 Signal-To-Noise Ratio	34
2.5.1 Required S/N for System Operation	36
2.5.2 Gaussian Noise Analysis	38
2.5.3 Predictions of Poisson Statistics	39
2.5.4 Interpretation and Application of Results	43
2.6 Effects of Atmosphere	49
2.7 Combined Effects of Atmospheric and Shot Noise	55
3. EXPERIMENTAL SYSTEM	56
3.1 Deflection Characteristics	57
3.1.1 DC Deflection Characteristics	59
3.1.2 AC Deflection Characteristics	60
3.2 Compensation for Hysteresis	62
Appendix A	66

LIST OF ILLUSTRATIONS

PART ONE

Figure		Page
1- 1	Cumulative deflection device.	2
1- 2	Size requirements for cumulative deflectors.	4
1- 3	Pulsed response of electro-optic deflector.	9
1- 4	Pulsed response of shear plate mirror deflector.	10
1- 5	Initial design of shear plate deflector, model SPM-1, with unit cell.	11
1- 6	Block diagram of experimental equipment showing polarization measuring circuit.	12
1- 7	Experimental setup for deflection and polarization measurements.	13
1- 8	Oscilloscope traces obtained during deflection measurements.	14
1- 9	Oven with thermocouple for measuring temperature effects.	15
1-10	Free-floating shear plate deflector, FSPM-1, with unit cell.	17
1-11	View of unit cell for ruggedized deflector.	18
1-12	Ruggedized shear plate deflector, SPM-8, with unit cell.	19
1-13	Autocollimator used in alignment of parts during assembly.	21

PART TWO

2- 1	Bradley error for tracking a corner reflector.	31
2- 2	Effective diameter of reflecting sectors of an optical corner reflector.	32
2- 3	Received laser power versus transmitter beamwidth.	34
2- 4	Signal to noise ratio versus transmitter beamwidth.	37
2- 5	Gaussian noise in low-pass and high-pass filters (after S. O. Rice).	40
2- 6	Noise in a low-pass filter.	42
2- 7	Estimated noise in a band-pass filter.	44
2- 8	Error rate versus signal to noise ratio.	48
2- 9	Atmospheric noise on return signal.	50

LIST OF ILLUSTRATIONS (continued)

Figure		Page
2-10	Probability of signal being forced below threshold by atmospheric noise.	53
2-11	Time spent below threshold on a single crossing.	55
2-12	Block diagram of bench test model.	57
2-13	Bench test model of acquisition and tracking system.	58
2-14	Close-up of transmitter.	59
2-15	Initial dc deflection curves.	60
2-16	DC hysteresis loops for SPM-4B.	61
2-17	AC deflection characteristics of a shear plate model beam deflector.	62
2-18	Hysteresis effects in a shear plate model beam deflector.	63
2-19	Electrical connections for series-capacitor deflection monitor.	63

PART ONE

DEFLECTOR DEVICES

1. INTRODUCTION

In the previous program under Contract NASw-731 it was determined that electro-optic refractors and shear-plate mirror reflectors could be designed to achieve deflection angles of approximately one degree for light beams with a minimum half-intensity beam angle of about 0.01 degree. These devices have the inherent capability for achieving deflection rates in excess of 10 kc/s, and they can be made to have relatively low light loss in spite of the use of large numbers of interfaces or mirrors. It was found that both the refractors and the reflectors required relatively large amounts of electrostatic energy to achieve maximum deflection, and the amount of energy is about the same for the two devices. The refractor, however, can be made to operate with much lower deflection signal voltages. The large energy requirements make it impractical to use these devices with wideband deflection signals extending into the tens of kilocycles per second. For structures using narrow-band deflection signals, however, the power required can be reasonably low even at very high frequencies, extending up to about 100 kc/s. It was concluded that rapid scanning of a two-dimensional field can be achieved by using saw-tooth modulated quadrature sinusoidal signals on tandem horizontal and vertical deflectors to trace out a spiral scan.

Precision deflection with these devices appeared to be feasible but difficult. It was evident that the temperature of the active elements (electro-optic crystals or piezoelectric ceramics) must be maintained constant to within a fraction of a degree, and that means would have to be found to compensate or correct for the nonlinear deflection experienced at high fields. Piezoelectric ceramics may pose special difficulties because these materials have characteristics that change slowly with the age of the material as the result of spontaneous depolarization. Furthermore, these materials are subject to partial depolarization when the applied voltage exceeds a certain threshold.

In the present program the results obtained previously have been extended to the development of deflector devices for a two-dimensional acquisition system for optical tracking of space vehicles from the launch pad. This work has involved a close examination of the characteristics and behavior of previously developed devices to ferret out weaknesses and limitations in the previous designs and to devise effective means for overcoming any such faults. The outcome of this effort has been the development of an improved deflector device, called the ruggedized shear plate deflector, which is described in Section 4.2. It appears that the design approach used in the development of this device will lead to deflectors suitable for the intended application.

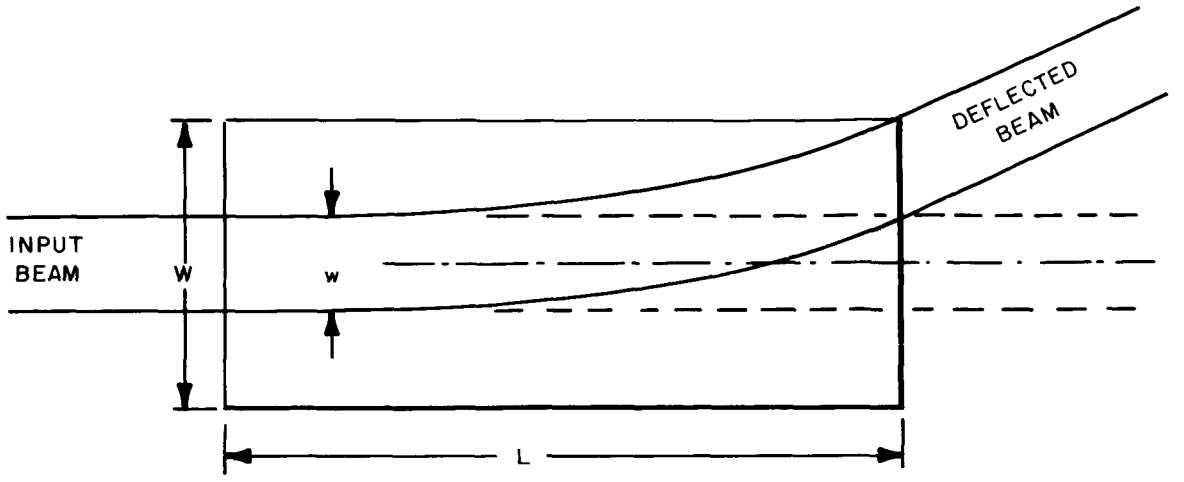

Fig. 1-1. Cumulative deflection device.

2. CHOICE OF DEVELOPMENTAL MODEL

Each of the two types of beam deflectors experimentally tested under the previous contract, the electro-optic and piezoelectric driven mirror, has qualities that make its use advantageous in certain applications. In this section the characteristics of each type are considered in the light of the present system requirements. These dictate the choice of a model best suited for further development.

2.1 THEORETICAL RESOLUTION LIMITATIONS

The resolution limitations of the above-mentioned devices and similar cumulative deflection devices are readily determined from the following analysis. The deflector is represented in Fig. 1-1 by a rectangular bar of length L and width W, which provides a maximum deflection per unit length K in response to the maximum deflection signal voltage applied to the device. A collimated laser beam of width w is passed lengthwise through the structure in the z direction and is gradually deflected upward, as shown by the solid lines, from its zero-voltage position, indicated by the dashed lines. For a given value of W and a given maximum value of K, we shall find the values for w and L which maximize the deflection resolution N, defined by

$$N = 2\varphi(L)/\theta_o, \tag{1.1}$$

where $\varphi(z)$ is the cumulative deflection angle obtained in passing a distance z through the structure, and θ_o is the half-intensity beam angle, given by

$$\theta_o = \lambda_o / w \tag{1.2}$$

where λ_o is the light wavelength.

The factor two appears in Eq. (1.1), because the beam can be deflected both upward and downward, using positive and negative deflection signal voltages. Thus, N represents the maximum number of distinct beam positions attained by the deflected beam.

By definition of K, we have:

$$d\varphi/dz = K. \tag{1.3}$$

But the deflection angle itself is

$$\varphi = \tan^{-1}(x/z) \cong x/z \tag{1.4}$$

for small angles. Integration of Eqs. (1.3) and (1.4), subject to the boundary conditions $\varphi(0) = x(0) = 0$, corresponding to the center ray of the beam, yields

$$\varphi(z) = Kz \tag{1.5}$$

and

$$x(z) = \tfrac{1}{2}Kz^2. \tag{1.6}$$

For a given structure length L, the resolution is maximized by making w just large enough so that the deflected beam grazes the upper corner of the structure. For this to happen,

$$x(L) = \tfrac{1}{2}(W - w). \tag{1.7}$$

Substitution of Eq. (1.7) into Eq. (1.6) leads to the following formula for w:

$$w = W - KL^2. \tag{1.8}$$

Combining Eqs. (1.8), (1.5), (1.2), and (1.1), we obtain the following formula for N, corresponding to this optimum value of w:

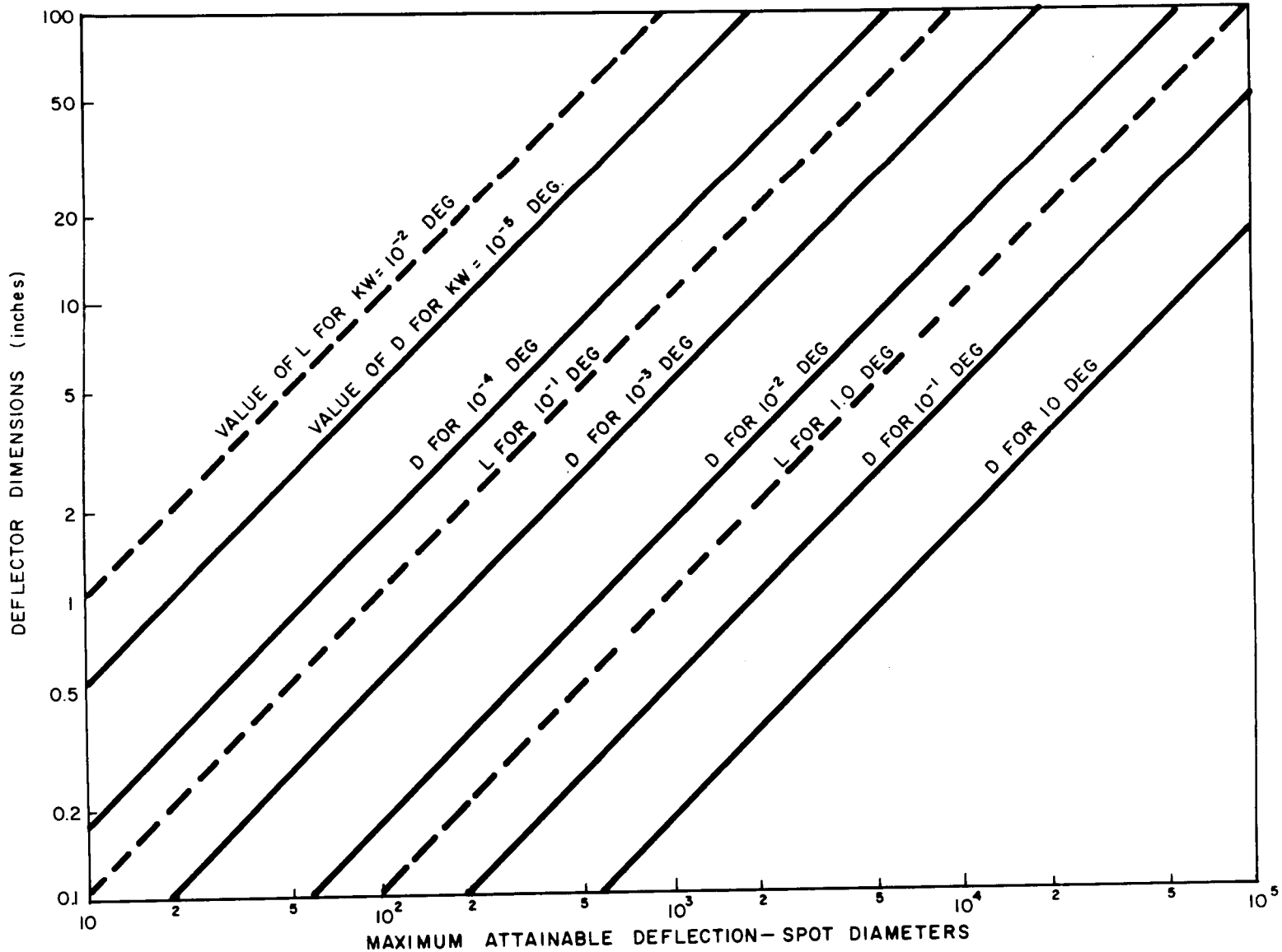

Fig. 1-2. Size requirements for cumulative deflectors.

$$N = 2KL(W-KL^2)/\lambda_o. \qquad (1.9)$$

Application of calculus reveals that this formula has a maximum for

$$L = (W/3K)^{\frac{1}{2}}. \quad \text{(collimated light)} \qquad (1.10)$$

The value of this maximum is

$$N_{max} = (16\ KW/27)^{\frac{1}{2}} W/\lambda_o \quad \text{(collimated light)} \qquad (1.11)$$

where KW, it will be noted, is the deflection per square section of the structure.

A somewhat more complicated analysis shows that slightly more resolution is obtained by passing converging light through the structure, making the input beam diameter equal to W, and arranging again that the output beam just grazes the upper corner of the structure. This provides an improvement by a factor of $\sqrt{2}$, so that for this case

$$N_{max} = (32\ KW/27)^{\frac{1}{2}} W/\lambda_o \quad \text{(converging light)} \qquad (1.12)$$

$$L = (2\ W/3K)^{\frac{1}{2}}. \quad \text{(converging light)} \qquad (1.13)$$

Figure 1-2 is a plot of Eqs. (1.12) and (1.13) which shows how large W and L must become to achieve a given resolution N with a given maximum value of the parameter KW. The largest value of KW that can be achieved in a cumulative deflection device suitable for operation at 2000 scans/second is about 0.1 degree, obtained with piezoelectrically driven mirrors in the shear plate configuration. In the type of tracking system under consideration here, where very high scan speeds are not necessary, this kind of deflector offers a distinct advantage over the electro-optic type with its higher frequency but lower deflection capability.

2.2 COMPARISON OF OTHER CHARACTERISTICS

A number of scan modes are considered in Part Two of this report, Two of them, the saw tooth scan and the triangular scan, require a deflector frequency response adequate to reproduce a few significant harmonics beyond the fundamental drive frequency. The electro-optic deflector is inherently capable of operation into the megacycle per second region, while a fundamental response limitation on the shear plate mirror unit is the first acoustic resonant frequency of the piezoelectric cube and mirror

assembly, about 100 kc/s. Since fundamental scanning frequencies will be limited to the low audio range it would seem that frequency response requirements pose no limitations on either type of reflector.

As far as precision of deflection and stability with temperature are concerned, both the electro-optic and shear plate mirror deflectors share the disadvantage of having highly temperature-sensitive active elements. In addition, the piezoelectric shear plate is subject to an aging process in which a change in characteristics slowly takes place due to spontaneous depolarization. There is, however, a technique of polarization measurement of deflection, described in a later section, which should render these drawbacks less severe.

Since the tracking system does not require the deflector to be in continuous use, and since the process of aging is very slow under normal temperature and electric field conditions, the deflector should remain stable over short periods, maintaining its accuracy with periodic calibrations. Thus, based on the foregoing resolution consideration, the shear plate mirror-type deflector is a good choice for further development.

In addition to meeting the basic requirements, the shear plate model has an additional characteristic which makes it more attractive. As will be discussed later, it is amenable to slight design modifications which will allow lower drive voltages, and consequently ease requirements on the scan amplifiers.

For these reasons the development program was concentrated almost exclusively on the shear plate mirror deflector.

3. CHARACTERISTICS OF EXPERIMENTAL DEFLECTORS

This section deals with the characteristics of shear plate deflectors using the piezoelectric ceramic PZT-4. The different effects are described and explained, and the techniques used to measure and overcome them are set forth.

3.1 HYSTERESIS

3.1.1 Effect of Hysteresis on Precision of Deflection

The phenomenon of hysteresis is common to all ferroelectric materials. The mechanism is the switching of domains of polarization within the material and exhibits itself as the familiar hysteresis loop when polarization is plotted against electric field. When these materials are used in a deflector such as the electro-optic (KDP) or the piezoelectric (PZT) model, the deflection also becomes a double-valued function of the applied voltage. Hysteresis, too, is inherently accompanied by an energy loss causing an internal temperature rise and an attendant change in the material characteristics.

A test was made by deflecting a laser beam across a slit in front of a multiplier phototube with the output of the phototube connected to the y-input of an oscilloscope and the deflection signal connected to the x-input. Two pulses were produced per cycle of the deflection signal: one with the beam scanning past to the right, and one with it scanning back to the left. For small scan angles, these two pulses were coincident on the oscilloscope, but they parted by an amount corresponding to more than one beam diameter at high signal levels. Tests of this sort have been performed on both types of deflectors, and both display the hysteresis characteristic of all nonlinear ferroelectrics. This effect is a more serious fault than simple nonlinearity, since the departure from linearity is not a single-valued function of the deflection voltage but instead depends upon the past history of the ferroelectric material.

3.1.2 Polarization Measurement of Deflection

It appears that there is a way to overcome this difficulty through use of polarization as a measure of deflection rather than voltage. It is likely that the deflection angle versus polarization is not a hysteresis curve, and it may even be quite linear. In the case of electro-optic refractors, it is known that the polarization vector P and the electro-optic constant r_{63} both have precisely the same temperature dependence (both following the Curie-Weiss law). This removes the problem of temperature control, for if polarization is used as a measure of deflection that measure will be correct even if the temperature changes. The fact that the temperature dependence of P and r_{63} are the same lends some credence to the supposition that these quantities have the same hysteresis curves.

To implement this, use is made of the fact that the charge on the electrodes of the deflector is indicative of the instantaneous polarization of the material. This charge may be measured by monitoring the voltage across a capacitor in series with the deflector. Actually the charge is proportional to the instantaneous dielectric constant

$$\epsilon = (1 + \chi_e)\,\epsilon_o \qquad (1.14)$$

where

$$\underline{P} = \chi_e\,\epsilon_o \underline{E},$$

in which $\underline{P}$ is the dipole polarization per unit volume and $\underline{E}$ the electric field. However, in most ferroelectrics $\chi_e >> 1$ and the susceptibility of free space may be neglected.

This technique has been verified experimentally using the method previously described of deflecting past a slit in a detector. The two pulses were made to merge for all positions of the slit along the scan line when the voltage axis measured polarization-derived voltage. To account for losses a resistor was used in parallel with the series capacitor. The value of the RC time constant was a function of frequency, tending to increase with frequency.

Experimental results on the effects of temperature on polarization measurement will be covered in section 3.3.2.

3.2 RESONANCE EFFECTS

3.2.1 Pulsed Operation

An initial investigation of the acoustic resonance characteristics of the different deflectors was carried out with high-voltage microsecond pulses. Pulses up to 30 kV were supplied from a magnetron hard-tube modulator of about a megawatt peak power rating.

Pulsed operation of one of the electro-optic deflectors with hyperbolic electrodes was obtained. Results indicate that ringing is not a dominant characteristic of the pulsed response of this device. Tests were performed by passing the pulse-deflected beam through a narrow slit into a wideband multiplier phototube and observing the output signal on an oscilloscope. The phototube was mounted on a rail so that it could be moved to various positions of the deflected beam. The deflection sensitivity appears to be about the same as that for low-frequency operation. Transient ringing was observed by placing the phototube near the edge of the undeflected beam so that even low-level deflection would change the amount of light intercepted by the phototube. The transient signal observed consisted of about 10 cycles at a frequency of about 125 kc/s. Oscilloscope traces of the beam response are shown in Fig. 1-3 for various positions of the phototube. It can be seen that the initial deflection (lower trace) follows the applied pulse (upper trace) quite well.

Pulses were applied to one of the shear-plate mirror deflectors, and it was found that an oscillatory transient deflection occurred with a ringing frequency of about 200 kc/s. The deflection sensitivity was about equal to the low-frequency value. The ringing frequency agreed with rough estimates of the lowest acoustic shear-wave resonance, obtained by dividing the shear-wave sound velocity by twice the maximum dimension of the shear-plate and mirror subassembly. Figure 1-4 shows the response of this deflector in the same manner as above. Deflection here does not follow the initial rise of the pulse as before and ringing is stronger and more persistent.

3.2.2 Structural Acoustic Resonance

When one of the original shear plate deflectors was operated in series resonance with an inductance bank in the frequency range of 1 to 10 kc/s, it was noted that at certain frequencies the device would deflect in two directions where only one was intended. The pattern formed by the deflected beam was a lissajous figure at these frequencies, becoming an ellipse near 6 kc/s. Some of the other frequencies were approximate submultiples of 6 kc/s. A plausible explanation for this is that the structure supporting the shear plate mirrors has a major acoustic resonance at about 6 kc/s and this resonance is excited by the sound generated by the piezoelectric cubes.

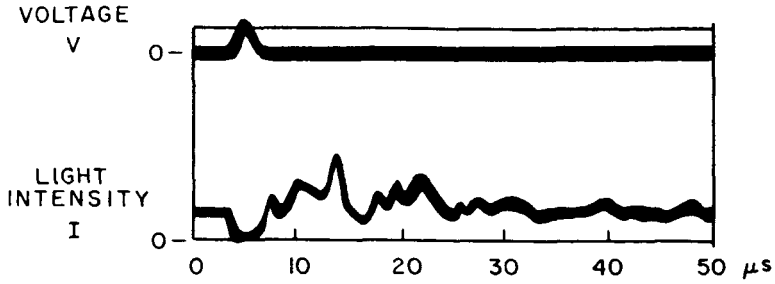

(a) Detector 0.8 inch to right of undeflected beam

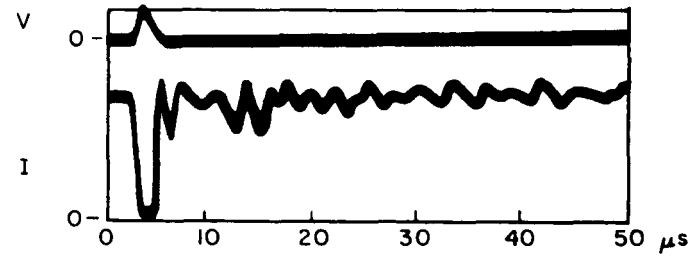

(b) Detector in position of undeflected beam

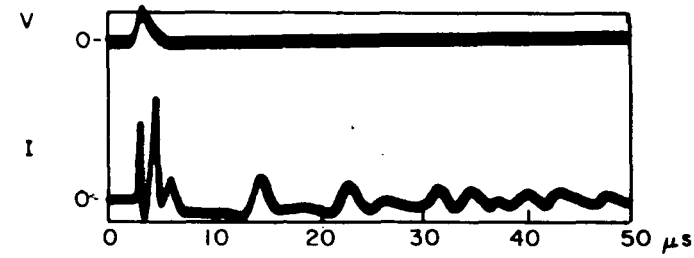

(c) Detector 1 inch to left of undeflected beam

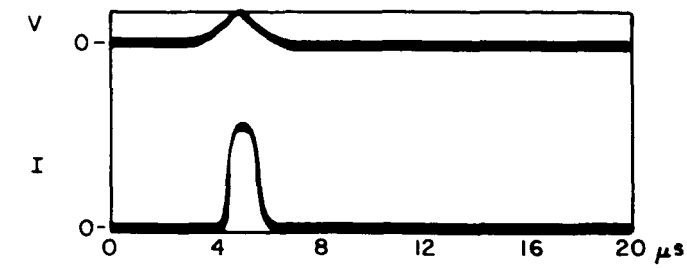

(d) Detector 2 inches to left of undeflected beam

Fig. 1-3. Pulsed response of electro-optic deflector.

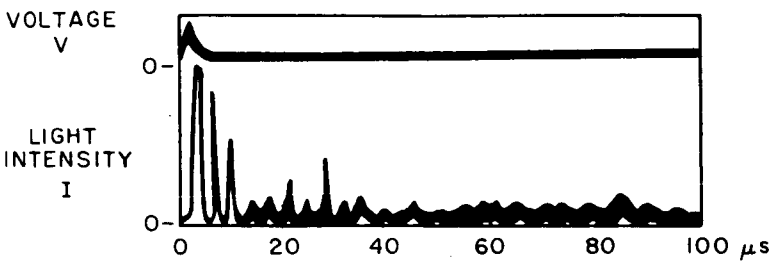

(a) Detector 2 inches to right of undeflected beam

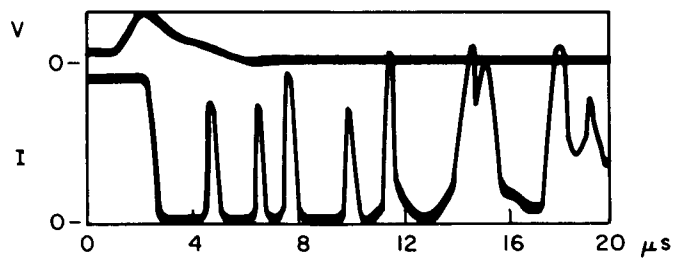

(b) Detector in position of undeflected beam

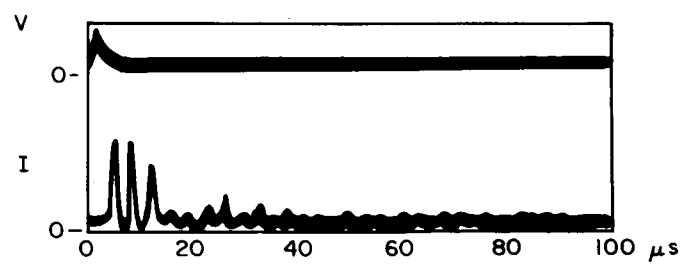

(c) Detector 2 inches to left of undeflected beam

Fig. 1-4. Pulsed response of shear plate mirror deflector.

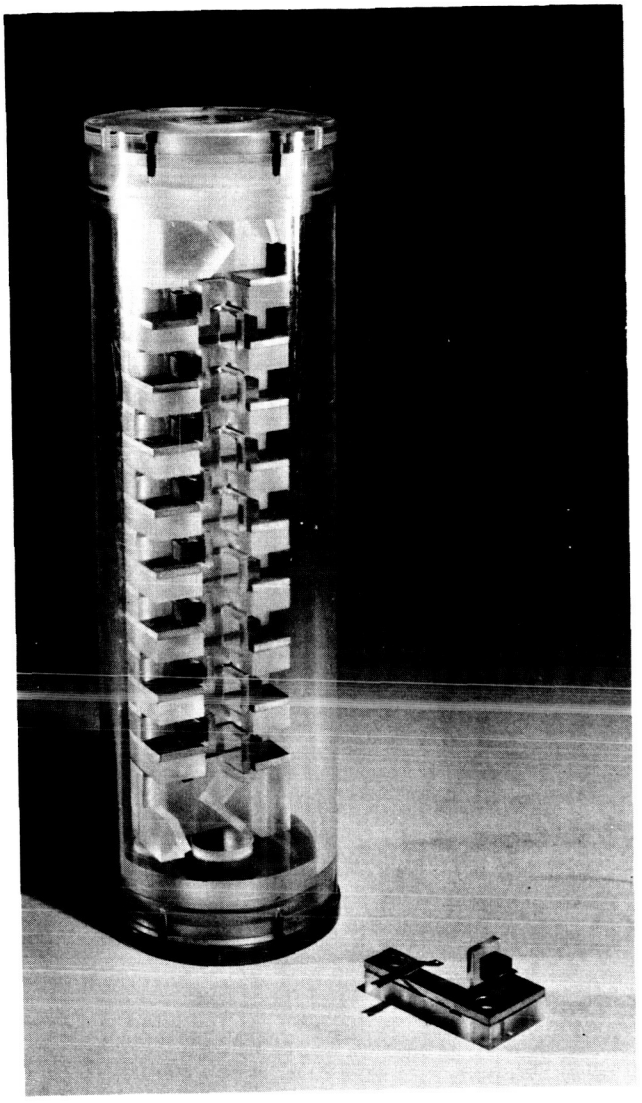

Fig. 1-5. Initial design of shear plate deflector, model SPM-1A, with unit cell.

The motion of the mirrors associated with this resonance is orthogonal to the direction of normal deflection. The superposition of this spurious motion upon the normal motion accounts for the two-dimensional pattern. Present also were resonances of the same origin which caused anomalous motion in the direction of deflection. Polarization in these instances was no longer indicative of deflection, and the onset of a resonance could be easily predicted.

This particular embodiment of the shear plate deflector is quite susceptible to mechanical resonances. As Fig. 1-5 shows, the members supporting the cubes are "L" shaped pieces of plastic which provide little mechanical rigidity. These pieces are also subject to plastic flow during maching operations, making it difficult to hold mechanical tolerances.

3.3 TEMPERATURE AND AGING EFFECTS

It is known from data supplied by the manufacturer that poled piezoelectric materials have deterioration characteristics that are functions of temperature and time after poling. What effect changes in piezoelectric constant, dielectric constant and dielectric dissipation with age and ambient temperature will have on deflector performance must be determined before operating conditions and system performance can be quoted. Accordingly, a test facility has been constructed where information on deflection sensitivity with age can be gathered in a consistent and repeatable fashion for all models. An oven is available to check performance under extended high-temperature conditions and to assess the effect of controlled-temperature gradients. These tests will also determine to what extent the measurement of polarization is a true indication of deflection.

3.3.1 Precision Deflection Measurements

The arrangement of equipment used for accurate determination of deflection and polarization under various conditions is given in Fig. 1-6 in block form and as a photograph in Fig. 1-7. The signal supplied by the

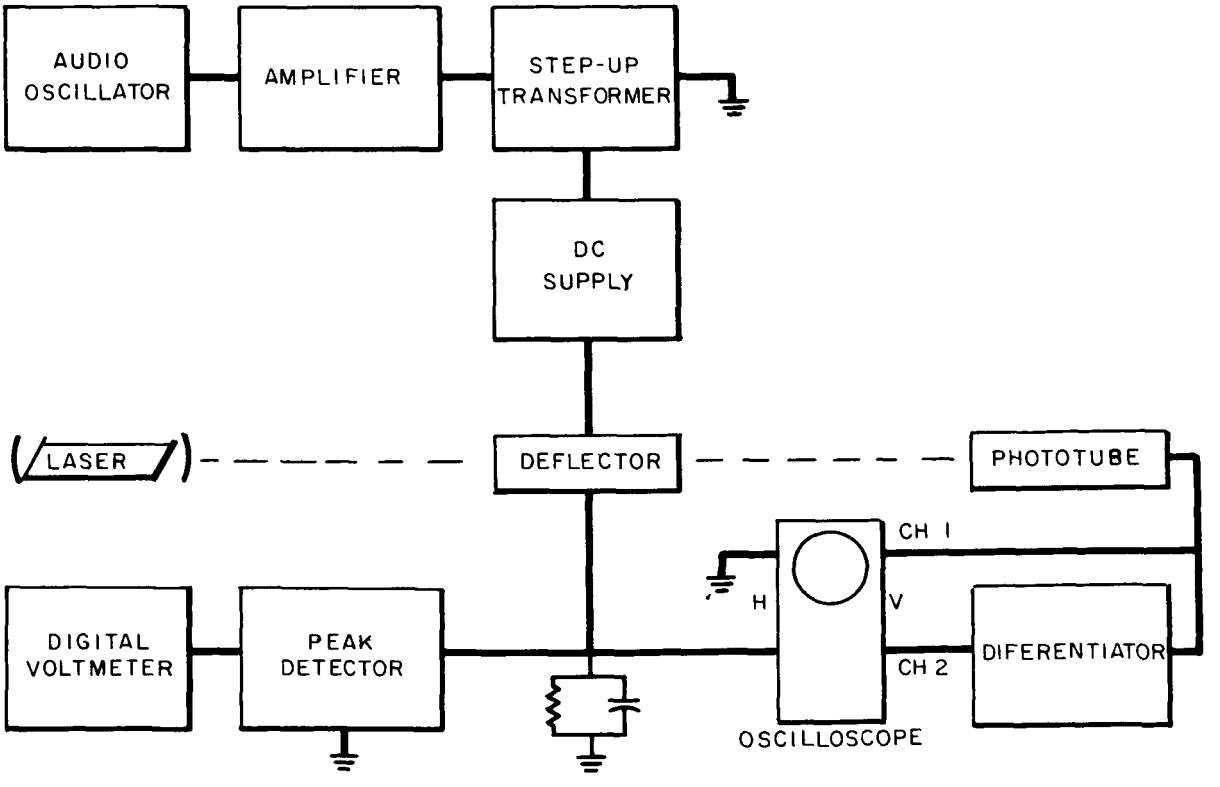

Fig. 1-6. Block diagram of experimental equipment showing polarization measuring circuit.

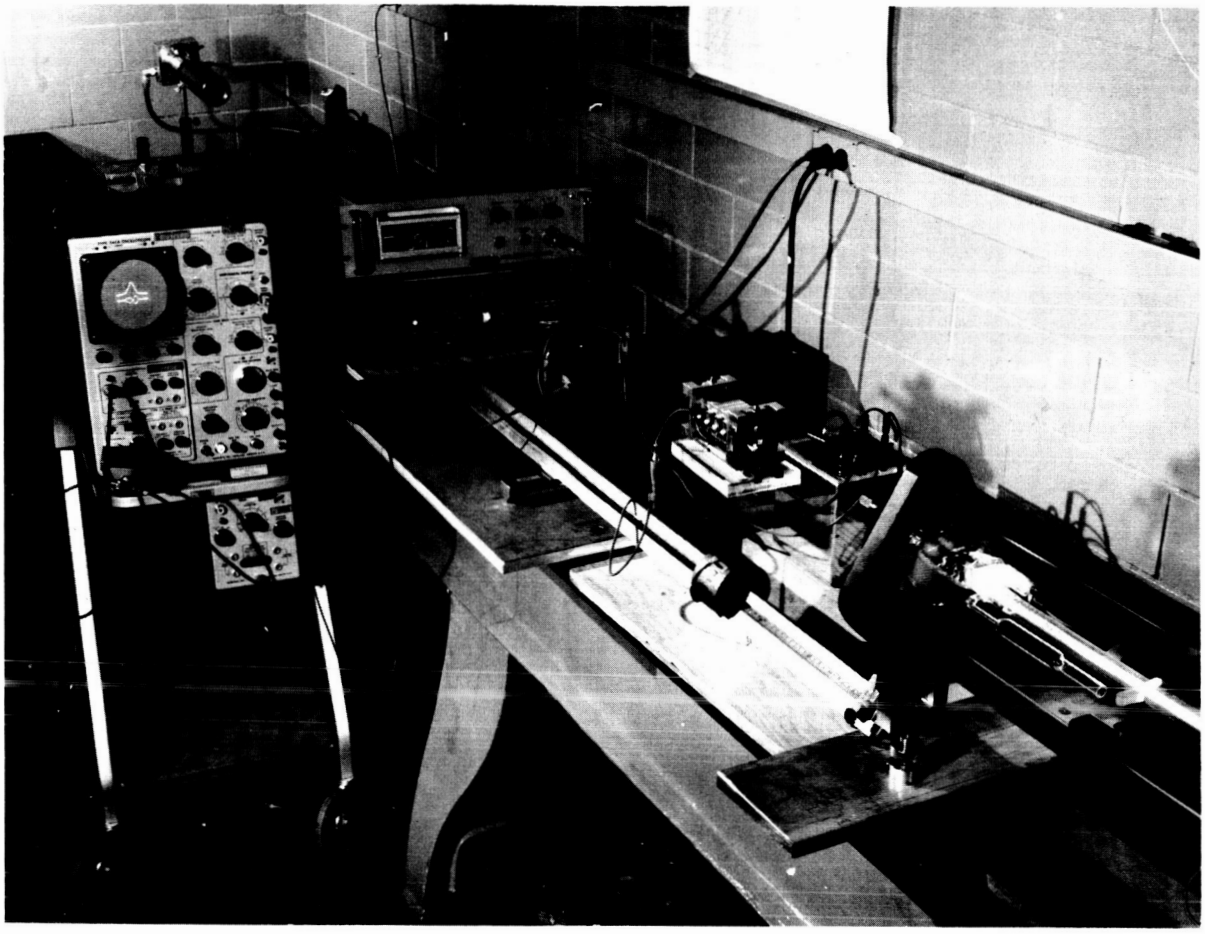

Fig. 1-7. Experimental setup for deflection and polarization measurements.

audio oscillator is amplified and put through a transformer to step up the voltage to about 5 kV peak from 30 to 1500 c/s. At higher frequencies the deflector is series resonated with an inductor to obtain high-voltage operation. This voltage is applied to the deflector in series with the polarization sampling circuit and a dc source. The signal on the polarization sampling capacitor is peak detected and read on a digital voltmeter. This same signal is also used to drive the horizontal axis of an oscilloscope.

Light deflected past a slit in the phototube is detected and applied to the vertical of the oscilloscope, directly into channel 1 and through a differentiator into channel 2. The traces during deflection appear as in part (a) of Fig. 1-8. A pulse of light occurs in the top trace as the beam crosses the slit (much smaller than the beam diameter). The lower trace, a differentiation of the upper one, consists of two curves which cross at the zero-slope point of the upper pulse. This corresponds to the center of the slit.

To obtain a set of points of deflection versus polarization, the zero point for no deflection is determined by applying a small ac voltage to the deflector such that the beam scans about half a beam diameter. The phototube is

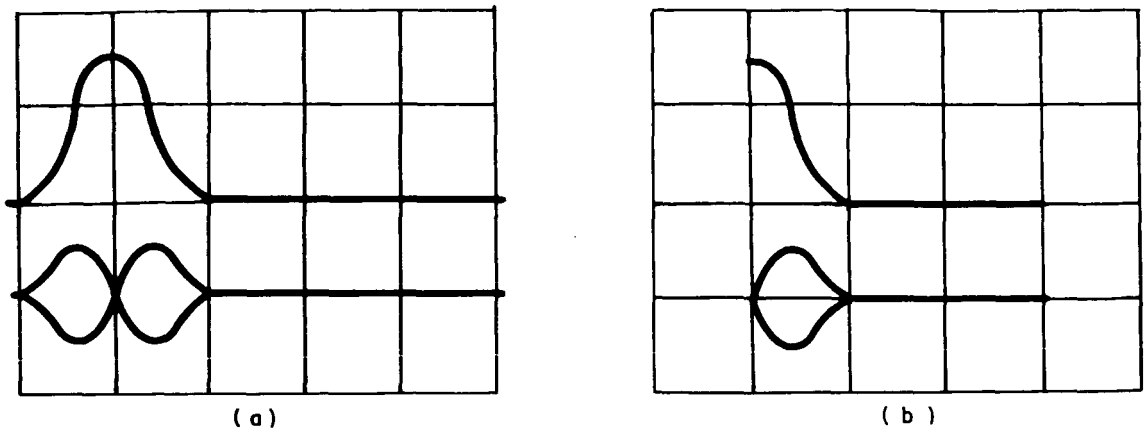

Fig. 1-8. Oscilloscope traces obtained during deflection measurements.

moved along a rail perpendicular to the beam until the skirts of the pulse on the oscilloscope are even. This is the zero point. From here the phototube is moved in increments perpendicular to the beam with a set of blocks cut in steps of one tenth of an inch. After insertion of a block, the voltage (and deflection) are increased until a pattern as in Fig. 1-8a appears. By adjusting the horizontal positioning of the oscilloscope, one of the vertical lines of the graticule can be made to lie directly on the intersection in the lower trace. If the voltage is now decreased to the point at which the edge of the upper pulse just touches this vertical line, as in Fig. 1-8b, the beam will deflect exactly to the center of the slit. The position of the slit is noted and the polarization voltage read from the digital voltmeter.

A measurement technique of this type is rapid and repeatable, yet accurate because the operator does not have to interpret distances or read scales. Accuracy is estimated to be better than one tenth of a beam position.

3.3.2 Temperature-Induced Drift

Measurements were made of the sensitivity and stability of deflection to changes in ambient temperature for the original models of the shear plate deflector. During an extended period of time in which data on deflection versus voltage and polarization were taken, it was noted that the undeflected beam did not return to the zero position immediately after a series of measurements had been made. Instead the beam would drift back slowly, taking about three minutes to reach zero. The amount of deviation from zero was a function of the voltage and frequency at which the deflector had been operating just previous to an examination of zero drift. A typical drift of 20 arc seconds per unit cell would occur both horizontally and vertically when the deflector had run at 4.5 kV peak and 2 kc/s for a short time.

The behavior of the structure seemed to indicate that internal losses in the piezoelectric cube were causing it to heat and expand nonuniformly, moving

the mirror through a slight angle; this effect has been observed with some piezoelectric single crystals under uniform heating.

This conjecture on the effect of heating was given support from the results of measurements of deflection sensitivity as a function of ambient temperature. An undriven shear plate deflector at thermal equilibrium in an oven at 40°C showed a zero drift of roughly 2.5 seconds/°C per unit cell as the oven temperature was lowered. Thus, a temperature rise of 8°C under maximum drive would account for the observed drift.

These latter measurements were performed using the nichrome wound oven seen in Fig. 1-9. As the deflector drifts from the zero position, a dc voltage is applied to restore it. The restoring voltage may then be related to the angular drift.

A method for dealing with this zero drift has been employed in the latest model of the shear plate deflector. Essentially, each cube has an image cube arranged such that thermal deflections cancel, while electrical deflections are cumulative. More will be said about this later.

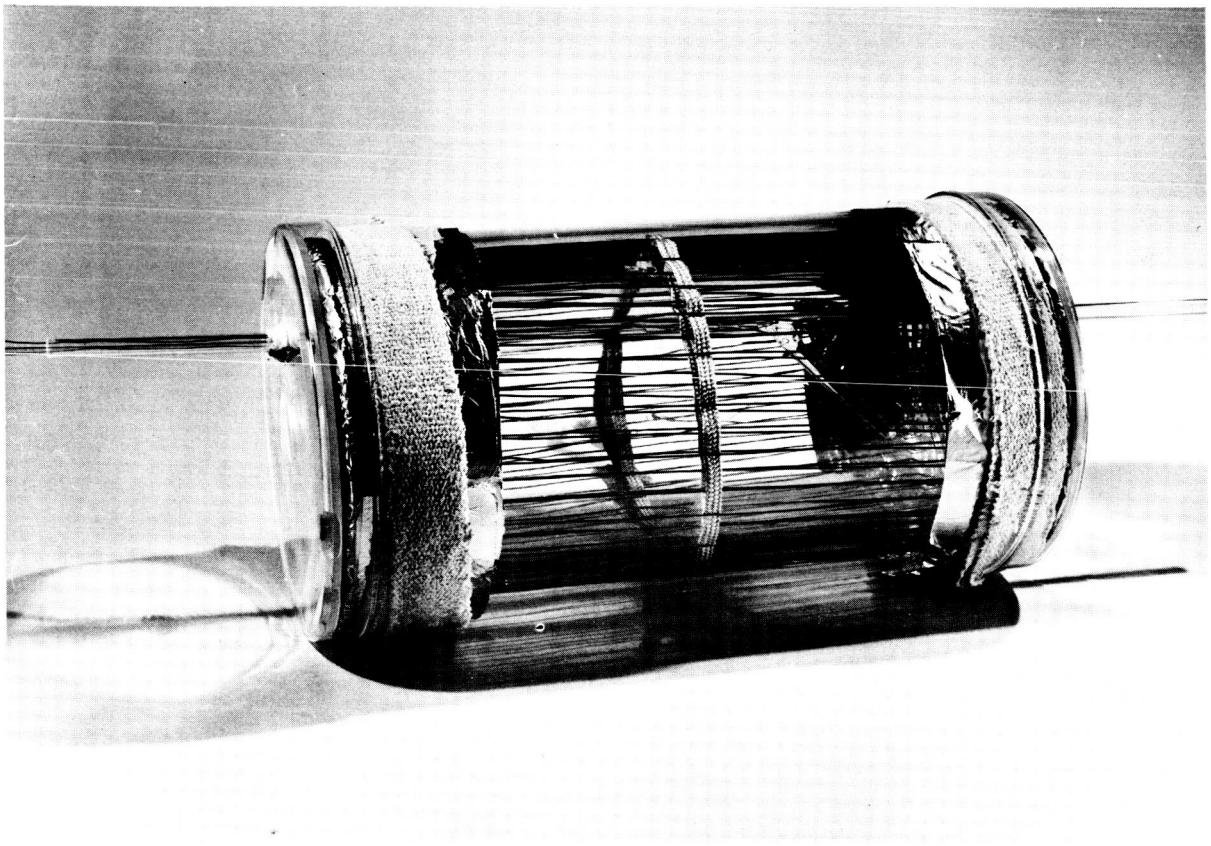

Fig. 1-9. Oven with thermocouple for measuring temperature effects.

3.3.3 Temperature Dependence of Deflection Versus Polarization

It was proposed that if polarization were a true measure of deflection, it should also be independent of temperature. Up to this time it has been difficult to obtain definitive data on this due to zero drift problems during measurement. Preliminary results indicate that over a temperature range of 5°C, polarization may be consistent with beam position to within one quarter of a beam width. It is planned to compare measurements of applied voltage and polarization voltage versus beam position over a range of temperatures to establish what type of linearity should be expected and the relationship between temperature, polarization and deflection.

3.3.4 Aging

The data obtained to date are not sufficient to make definite predictions about what effects aging will have on voltage sensitivity of deflection, polarization, temperature dependence, losses, etc. Records have been kept of deflection, capacitance and dissipation factors for certain units and will be evaluated periodically throughout the test period.

4. DEVELOPMENT OF NEW DEFLECTORS

4.1 SYMMETRICALLY SUPPORTED MIRROR DEFLECTOR

A new design was devised for mounting the deflector shear plates and mirrors to eliminate the transfer of acoustical energy to the supporting structure. The design philosophy called for the piezoelectric shear-plate to be supported at a point at which the shear strain is zero such that no mechanical motion will be transmitted to the support. This point must, then, be a node of vibration of the shear-plate mirror unit. By placing mirrors on four sides of the shear-plate cube instead of one, a symmetrical structure results in which the shear vibrational node is on axis through the centers of the remaining two sides. Support of such a unit would come from two point contacts made at the center of the symmetry forces. Each individual subassembly would then be "free floating" in the sense that it is acoustically isolated from the entire structure.

In addition to eliminating unwanted resonances, it was felt that the new design would yield other desirable features. Normal resonances existing in the subassemblies will be easier to predict and control due to the simpler geometry. Alignment problems associated with the mirrors would be greatly reduced since each set of mirrors can be individually adjusted after mounting. There are to be two adjacent functional mirrors on each subassembly, the other two being dummies. These appear as an outside corner reflector having the property of being rather uncritical with respect to angular orientation.

Such a deflector was built and is shown in Fig. 1-10. Each cell of this structure is supported by two dowels inserted in shallow holes centered on opposite faces of the piezoelectric cube. This method of support is

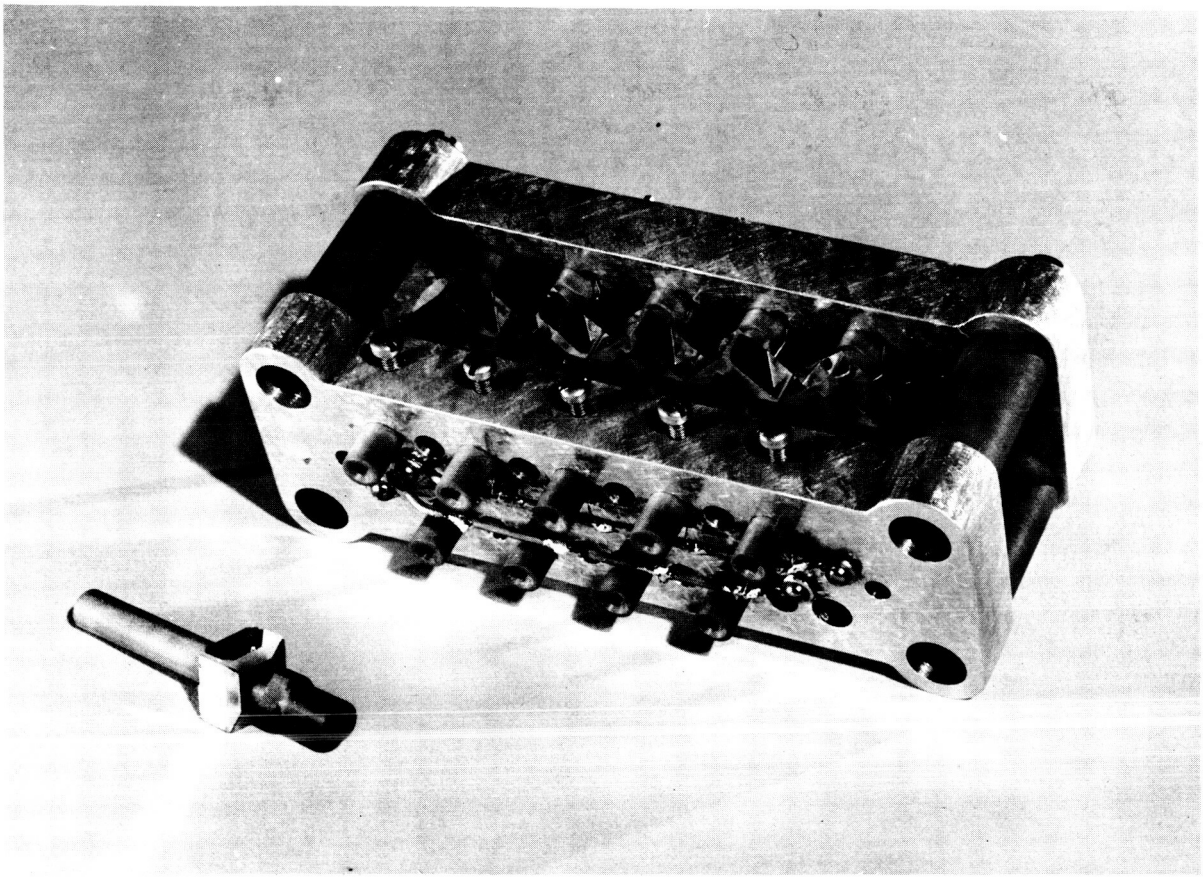

Fig. 1-10. Free-floating shear plate deflector, FSPM-1, with unit cell.

consistent with the design criterion only if the effect of the holes can be neglected. Proper hole size was determined by measuring the resonant Q of single piezoelectric cubes as a function of hole size with the cube isolated and, again, with the supporting dowel inserted. By comparing the Q's of the major resonance with and without the dowels, the amount of power transferred to the support can be determined.

Measurements of Q set the hole size at no more than 60 mils. Subsequent evaluation of the completed model showed this to be too small for proper vibrational stiffness. Two dimensional deflection was still a problem and alignment was not as simple as was first believed. In view of this it was decided to put further effort into a ruggedized version of the first design. Details are given in the following section.

4.2 RUGGEDIZED SHEAR PLATE MODEL

In the preceding sections some of the more important problems encountered in the design of a precision shear plate deflector were discussed. In the latest version of the deflector an attempt was made to overcome these problems through a better understanding and more sophisticated design.

4.2.1 The Unit Cell

The basic unit cell consists of a mirror and PZT-4 shear plate bonded to a support, as shown in Fig. 1-11. The support was fabricated from aluminum in the form of a yoke to increase mechanical strength, and the cube is placed in a frame which has high vibrational stiffness. This effect is enhanced by the adjacent frames in the assembly. In this way it has been possible to eliminate unwanted modes of deflection caused by structural resonances.

The method used to detect the presence of deflection perpendicular to the normal mode uses the same arrangement of equipment as was shown in Fig. 1-6. The slit covering the phototube, however, is arranged to lie parallel to the scanned line with the edge of the line just grazing the edge of the slit. If any light falls into the phototube due to perpendicular deflection, a pulse will be seen on the oscilloscope at the corresponding point. The ruggedized assembly was tested in this way from 0.1 to 10 kc/s with no anomalous behavior noted.

It is desirable to be able to drive the deflector directly from an amplifier without the use of a voltage step-up transformer and its inherent frequency limitations. One way of reducing the high-voltage requirement is to build up the piezoelectric shear element from a number of slices, with the electrodes sandwiched between the slices. In a four-slice element, for instance, the voltage applied to these electrodes need only be one quarter as much as that needed to cause identical shearing action in the same size solid element.

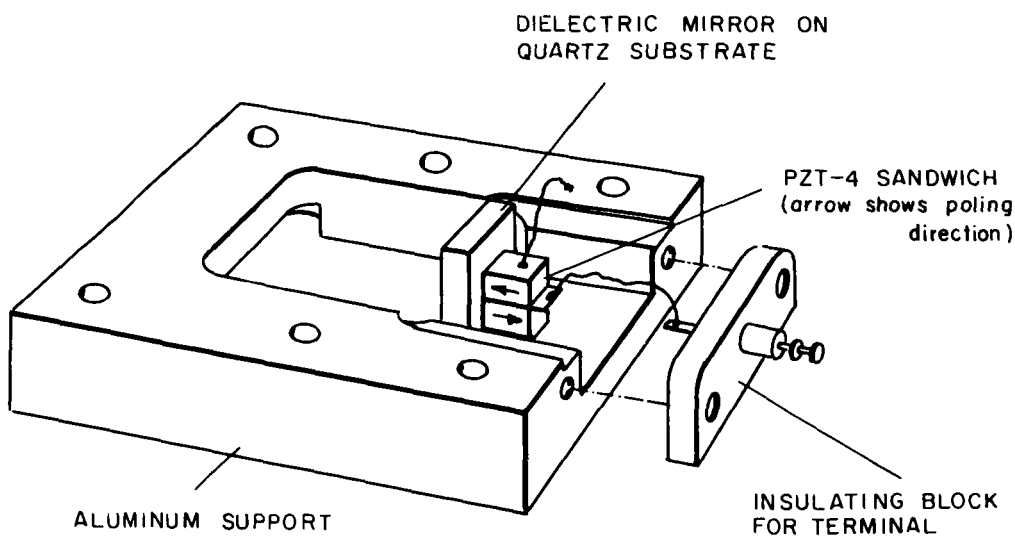

Fig. 1-11. View of unit cell for ruggedized deflector.

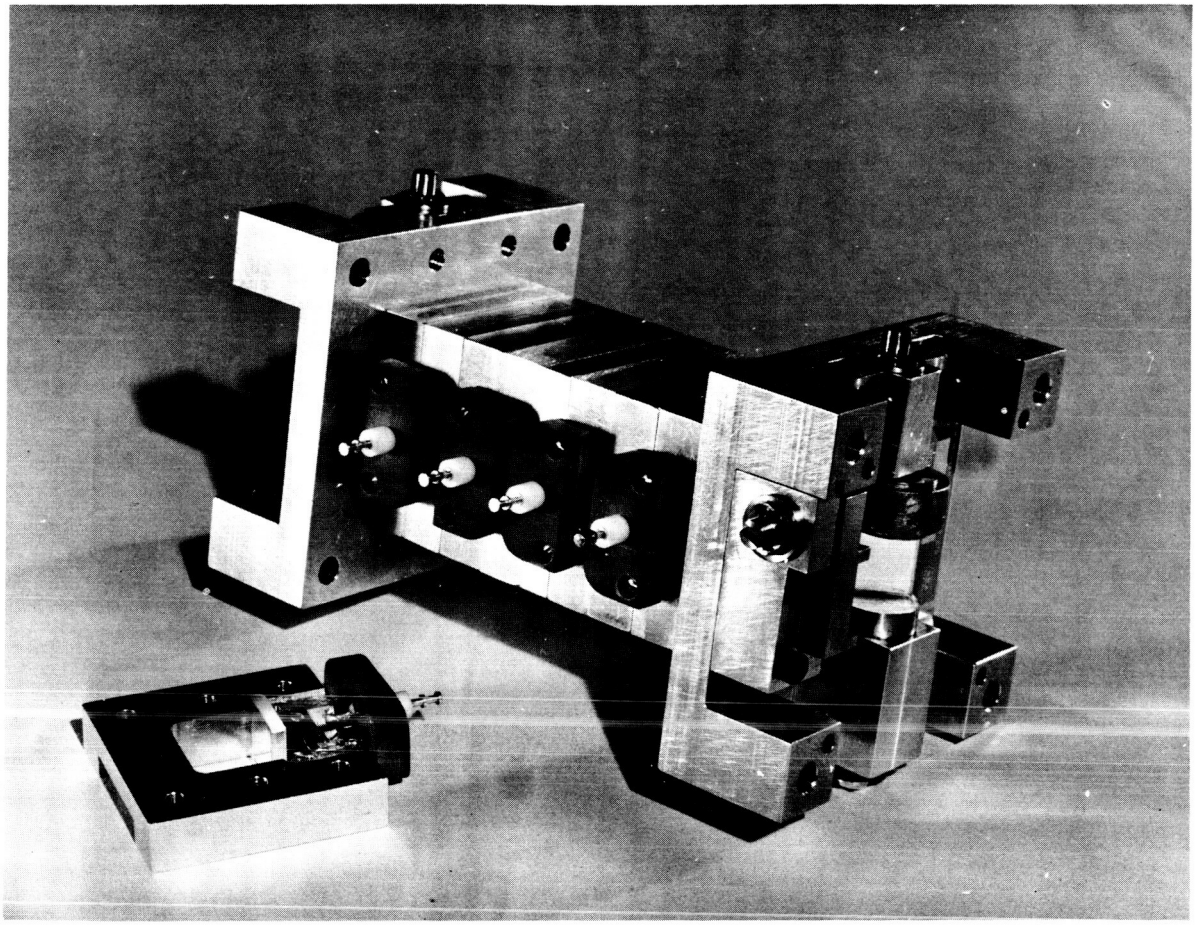

Fig. 1-12. Ruggedized shear plate deflector, SPM-8, with unit cell.

These modifications were incorporated in the latest ruggedized model. The drawing of Fig. 1-11 depicts the two slice sandwich used for that shear element. The top and bottom electrodes are grounded to the frame while the center electrode is brought out to a terminal. The poling direction of alternate slices must be reversed if the field directions are to cause complimentary shearing in each slice. A six slice element seems practical at this point, bringing the peak drive voltage to about 800 V.

4.2.2 Balancing of Thermally Induced Motion

Temperature changes in the shear elements due either to internal losses or changes in ambient temperature have caused the zero position of the undeflected beam to drift. This action, while not yet completely understood, has been considerably reduced in the ruggedized version through the use of a symmetrical design.

The assembled structure has a mirror plane of symmetry at its center, as is evident in Fig. 1-12. This construction allows thermally induced deflection in the first half to be canceled by similar but oppositely directed

response in the second half. The field directions are reversed in the two halves to provide additive voltage deflection. A temperature rise of 20°C in this structure was accompanied by a drift of approximately 0.3 sec/°C for each unit cell. It is probable that this amount can be attributed to a lack of complete uniformity among the unit cells.

4.2.3 Construction Techniques

Much effort has been applied to assembling a deflector whose mechanical tolerances were known and controlled, insuring full use of all mirrors by the laser beam. Mating surfaces of each aluminum yoke were lapped flat and parallel. The yokes are provided with locating pins so that no angular error is introduced in assembly and parts may be dismantled and reassembled in any order. End sections with mirrors adjustable in two planes let the beam enter and leave coaxially and allow correction for any residual deflection.

Slices of PZT-4 for the active element are cut from a disk, obtained from Clevite Corporation, and are ground flat and parallel. A 2000-Å layer of nickel is evaporated on each of the large surfaces to serve as electrodes. At this point and after each subsequent operation, the capacitance and dissipation factor of each of the slices are recorded.

Pairs of slices are then bonded together with an epoxy. A 2-mil copper tab included in the sandwich protrudes and serves as a center electrode (see Fig. 1-12). The capacitance measurement here serves also as an indication of faulty electrical coupling of the copper electrode to the slice. The front of the resulting cube is then ground flat and attached with an epoxy to a dielectric mirror on a quartz substrate. Assembly of the cube-with-mirror to the yoke is observed through an optical collimator (Fig. 1-13). Final corrections may be made at this point. Pins in the collimator platform locate the yoke and reference this operation to the assembled structure.

4.2.4 Experimental Results

Two units of the ruggedized shear plate deflector were constructed, and are referred to as models SPM-7 and SPM-8. Because of an error in assembly, the PZT-4 slices making up the shear elements in SPM-7 were oriented with their poling in the same direction. This unit was converted to operate in the normal manner with field applied across the two slices in the same direction.

Deflection sensitivity for SPM-8 at 200 c/s was 0.086 degrees/kV as compared with 0.097 degrees/kV for a previous model SPM-2 with the same number of cells. This difference is not totally unexpected. The thin layer of epoxy used to bond the slices together acts as a capacitor in series with the slice, reducing the capacitance of the sandwich by about 1.2 percent. The voltage developed across this layer reduces that available to cause shear in the slice. This will become more pronounced in the six stack element.

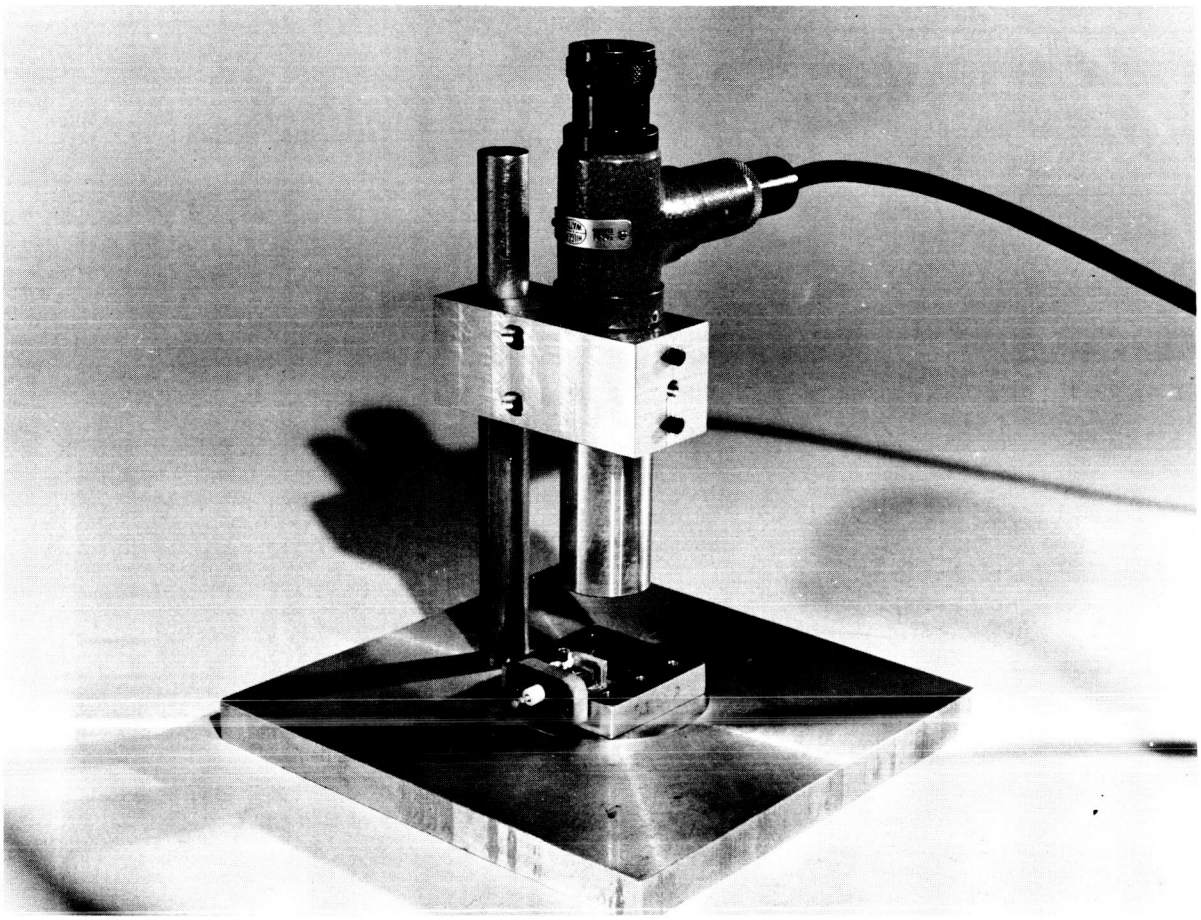

Fig. 1-13. Autocollimator used in alignment of parts during assembly.

As mentioned previously resonances from 0.1 to 10 kc/s have been eliminated, and progress is being made in solving the problems of thermally induced deflection. It was noted recently, however, that a change in temperature causes the mirrors to warp slightly into a concave configuration, giving rise to a focusing action on the beam. It is likely that this and thermal drift are related so that they may be handled in similar ways.

5. CONCLUSIONS

It has been concluded that the best approach to developing a deflector for use in the tracking system discussed in Part Two is through the ruggedized shear plate mirror type deflector. Among the advantages of this type of deflector are its relatively high speed of response and mechanical and chemical stability. A low light attenuation can be expected, and the voltage requirements may be reduced through the stacking type of construction for the active element.

There remains a number of recognized problems which must be resolved. Among the most important of these are the thermally induced drift and beam focusing. Symmetry of design is now being employed as a partial solution with encouraging results. A second possibility is use of materials with matching expansion coefficients. Electrical breakdown across the ceramic surface is still present at the higher voltage levels but this provides no basic limitation on deflector performance.

Fundamental questions on the seriousness of aging, temperature dependence of deflection sensitivity, and causes for thermal motion and defocusing are yet unresolved. The importance of these effects are, of course, reduced when the deflector is used only for short periods so that it may be recalibrated at the start of each period.

PART TWO

BEAM DEFLECTOR SYSTEMS

1. INTRODUCTION

The material reported in this section is divided into two major tasks: system analysis for applications of high-speed beam deflectors, and bench tests of the devices over a total two-way distance of approximately 630 yards.

The system analysis task was designed to examine the uses, potentialities, and most favorable means of employment of the beam deflectors in accomplishing optical acquisition and tracking. To this end, various possible scan modes were formulated and their individual characteristics examined for potential use in systems. A detailed analysis was made of one possible type of system application, the tracking of a retro-reflector on a moving target. The results of these system calculations are sufficiently general that only slight modifications are necessary to apply them to a variety of possible systems. Because successful use of such contemplated systems is intimately related to the magnitude of the received signal and to the various sources of noise encountered in such an application, a section is included which encompasses such received power and signal-to-noise calculations. Also included is a discussion of the effects of a turbulent atmosphere on system accuracy and the required signal to noise ratio as a function of the probability of missing the target return in a single acquisition cycle.

The bench test portion of this work had two goals: to examine the characteristics of the beam deflectors for a fairly long path to provide a fine-grained look at their peculiarities, and to provide an experimental "feel" for the devices to assist in formulating applications for them. For these tests the laser, beam deflectors, and receiver were located in the engineering laboratories with a clear view to the end of Sylvania's property. A corner reflector was located approximately 950 feet distant, at which range one minute of angle covers an area 3.32 inches wide. The receiver consisted of a 6-inch diameter, 48-inch focal length mirror and a 1-inch focal length eyepiece suitably mounted so that the return energy is collimated after passing through it. The beam is then split, with half going to an 8 power telescope with cross hairs for ease of alignment and the other half to a detector through a lens, filter, and field stop. This receiver has proved to be an excellent arrangement and is easily aligned.

The investigations to date indicate that successful systems to accomplish acquisition and tracking can be built employing beam deflectors. Characteristics of such systems and directions future work on beam deflectors should take to build these systems are described in this section of the report.

2. SYSTEM ANALYSIS

2.1 BEAM DEFLECTORS AS SYSTEM COMPONENTS

The beam deflectors may be used either on the transmitting end where they may be followed by an optical system or on the receiving end where they are preceded by optics. In either case the scan angle can be changed by a change in the focal length of the optics. However, an increase in the angle of scan is necessarily accompanied by an increase in the beamwidth. The large apertures required on the receiving optics for light gathering power necessitates long focal lengths and small scan angles. The transmitter, however, seldom has need for such large apertures and therefore retains greater flexibility in the control of scan angle. In either situation the number of beam positions deflected by the beam deflector remains constant. Because of this inherent characteristic, the deflectors will probably be useful on the receiver only for applications such as tracking scanning when only small deflections are necessary. For this type of function, other devices such as image dissectors and spinning reticles are highly developed.

On the transmitter, however, the beam deflectors fulfill a requirement that has not been satisfied by any other device. Use of the beam deflectors allow the transmitter to participate in an acquisition mode where little time can be allowed to establish contact with a target even though the position of the target is now well known.

The following describes the manner and systems in which the beam deflectors can be used in an optical acquisition and tracking system.

2.2 SCAN MODES

There are a number of possible scan modes which can be conceived to accomplish the acquisition and tracking functions. The mode which would be selected for use in a given system will be chosen on the basis of a number of inter-dependent parameters of which the beam deflector characteristic is only one. The following is a discussion of four possible acquisition modes which could be accomplished with a beam deflector. In this discussion it is assumed that an overlap is desirable between successive scans to minimize the chances of missing the target and that the transmitter beamwidth may be different than the receiver instantaneous field of view. Because the range attainable with an optical system is so intimately associated with the transmitter beamwidth, the scan mode calculations will be expressed in terms of that parameter rather than the receiver field of view. In cases where the receiver field may be less than the transmitter beamwidth, an appropriate proportion function is used.

2.2.1 Sawtooth Scan

The sawtooth scan mode assumes a square acquisition field in which the beam is swept in successive lines, each displaced from the next by an

increment proportional to the beamwidth. This type of scan, similar to a television scan, employs a fast sawtooth at the line scan rate and a slow sawtooth in the orthogonal direction at the frame scan rate. The reciprocal of the frame scan rate is the acquisition time.

The number of beam positions in a scan line is $n = \varphi/\theta_T b$ where φ is the total acquisition angle and $b = \theta_R/\theta_T \leq 1$

θ_T = Transmitter beamwidth

θ_R = Instantaneous angle of receiver field

The number of scan lines in the total field is $\varphi/p\theta_T b$ where "p" is the fractional part of the beamwidth the scan overlaps.

The total effective number of beam positions, therefore, is

$$N = \frac{\varphi^2}{\theta_T{}^2 p b^2}, \tag{2.1}$$

and the dwell time t_d is

$$t_d = \frac{T_A}{N} = \frac{p\,\theta_T{}^2 b^2 T_A}{\varphi^2}, \tag{2.2}$$

where

T_A = frame period or acquisition time.

The dwell time may be determined by receiver bandwidth or, as will be later developed, by the transit time of the light between transmitter and receiver.

2.2.2 Triangular Scan

Limited frequency response of the beam deflectors may make a fast retrace such as needed in a sawtooth drive impossible to attain. A modified raster scan, therefore, would employ a triangular driving waveform. Because overlap of the same fraction, p, is necessary in all parts of the scan, the effective slow retrace has the effect of doubling the effective number of beam positions, and thus halves the dwell time.

The dwell time for the triangular scan is, therefore,

$$t_d = \frac{T_A}{2N} = \frac{p\theta_T^2 b^2 T_A}{2\varphi^2} . \qquad (2.3)$$

2.2.3 Sinusoidal Scan

This scan employs a sinusoidal drive at the line rate, but a ramp or sawtooth at the slower frame rate. Unlike the previously described scan modes, the dwell time varies at different places on the scan line.

The motion of the spot in each scan line has the form

$$y = y_o \cos \omega t$$

The velocity, therefore, is the differential of this expression, or,

$$\frac{dy}{dt} = \omega y_o \sin \omega t$$

and the maximum velocity,

$$v_{max} = \omega y_o = 2\pi f y_o = 2\pi f n \ \frac{\text{beam positions}}{\text{second}}$$

where

$$n = \text{number of beam positions/scan line}$$

The minimum dwell time, then, is

$$t_d = \frac{1}{v_{max}} = \frac{1}{2\pi f n} = \frac{\theta_T b}{\varphi 2\pi f} .$$

Since

$$f = \frac{\varphi}{pb\theta_T T_A}$$

$$t_d = \frac{p\theta_T^2 b^2 T_A}{2\pi\varphi^2} . \qquad (2.4)$$

It will be noted that this dwell time is a factor of 2π shorter than that of the raster scan.

2.2.4 Spiral Scan

A scan form that is still easier to use to drive the beam deflectors is a spiral scan which uses only amplitude-modulated sinusoidal signals.

The two tandem beam deflectors are driven in phase quadrature with sinusoidal signals of increasing amplitude. The beam then moves from the center to the outer edge in a spiral pattern. The equation of such a spiral takes the form

$$R = k\alpha$$

and

$$p\theta_T b = 2\pi k$$

where k = constant, α = angle in polar coordinates, and R = angular distance from the center.

Thus,

$$R = \frac{p\theta_T b}{2\pi}\alpha .$$

The average length of the i^{th} cycle is $L_i = 2\pi R_i$, where R_i is the average radius between the $(i - 1)^{th}$ cycle and the i^{th} cycle, or

$$R_i = \frac{1}{2}\left[p\theta_T b\,(i - 1) + p\theta_T bi \right] = p\theta_T b\,(i - 0.5).$$

Thus,

$$L_i = 2\pi p\theta_T b\,(i - 0.5).$$

The number of beam positions in L_i is simply

$$m_i = \frac{L_i}{\theta_T b} = 2\pi p\,(i - 0.5).$$

If i_T is the total number of cycles in the scan pattern, the time per cycle is

$$t = \frac{T_A}{i_T} .$$

The minimum dwell time will occur in the final cycle, and will be equal to

$$t_D = \frac{t}{m_{i_T}} = \frac{t}{2\pi p\,(i_T - 0.5)} = \frac{T_A}{2\pi p i_T\,(i_T - 0.5)}$$

or

$$t_D \approx \frac{T_A}{2\pi p i_T^2}$$

If the total number of beam positions across the field of view is $n = \varphi/\theta_T b$, then allowing for an overlap of successive cycles, the total number of cycles is

$$i_T = \frac{n/2}{p} = \frac{\varphi}{2p\theta_T b} .$$

Substituting this equation into the equation for t_D gives, finally,

$$t_D = \frac{2T_A\theta_T^2 p b^2}{\pi\varphi^2} . \qquad (2.5)$$

This dwell time is less than that of the raster scan by a factor of $2/\pi$.

2.3 SYSTEM TO ACQUIRE AND TRACK A CORNER REFLECTOR

A system that positions the transmitter and receiver at a common location and tracks a cooperative reflector on a moving target is one of interest. This system will be discussed specifically, but most of the characteristics are common to a large number of possible systems.

If the target is moving and is some distance from the acquisition and tracking system, the finite transit time of the signal from the transmitter to the reflector back to the receiver may have an effect on system operation. For example, if the dwell time as calculated in the previous section is shorter than the two-way transit time, and if the receiver has an instantaneous field of view no larger than the transmitter, the return signal can never be detected by the receiver. This, of course, assumes that the receiver and transmitter are scanning in unison. When this condition occurs, two possible solutions are evident: the receiver can be made to lag the transmitter scan by an

appropriate amount, or both beams can be enlarged so that the dwell time is sufficiently lengthened.

The first solution assumes knowledge of the range to the target but will be a necessary recourse in many situations. The second, involving widening of the beam, will be discussed in this section.

Another system constraint imposed because of the target motion is that the total acquisition time must be short enough that the angular motion of the target is sufficiently small to be insignificant.

The above conditions, therefore, place the following boundaries on the contemplated system:

$$t_d = \frac{2aD}{c} \tag{2.6}$$

where

a = number of transit times in one dwell time

D = range to target distance

c = velocity of light

$$T_s = \theta_T bg/V, \text{ in which} \tag{2.7}$$

g = fractional part of θ_T missile moves during $T_A (0 < g < \varphi/2\theta_T)$, and v = angular missile velocity in radians/second.

If these two boundary conditions are inserted into Eq. (2.2) the minimum transmitter beamwidth which will satisfy the stated conditions is:

$$\theta_T = \left[\frac{2\,a\,D\,v\,\varphi^2}{p\,b^3\,c\,g}\right]^{\frac{1}{3}} \text{ radians} \tag{2.8}$$

The raster scan frequency, in scans/second, is

$$f = \frac{\varphi}{\theta_T T_A p b} = \frac{1}{b}\left[\frac{vc^2}{4\,g\,p\,\varphi\,a^2 D^2}\right]^{\frac{1}{3}} \tag{2.9}$$

A similar analysis using the other scan modes reveals that the term in the brackets in Eq. (2.8) will increase in the same ratio as the dwell time decreases from the raster scan case.

The minimum allowable value of θ_T, therefore, for triangular scan is $(2)^{1/3}$ greater than that for raster scan. Section 2.4 will discuss the maximum value of θ_T that is allowable on the basis of range, available power, and other system characteristics. A given system must employ a value of transmitter beamwidth between these two limits; in general, the beamwidth chosen will be the minimum rather than the maximum in order to maximize the signal to noise ratio.

2.3.1 Bradley or Transit Time Error

Angular errors introduced when there exists a transverse component of velocity between source and receiver are well known, and were first described by Bradley in the 18th Century.

A special case arises when the transmitter and receiver are at the same location and a transverse velocity component exists between them and the retro-reflector. Consider the geometry of Fig. 2-1. M represents the position of the corner reflector and 1 the position of the transmitter at time 0. Because only relative motion is of importance, assume the corner reflector to be stationary while the transmitter-receiver moves. The signal takes a time $t_t = D/c$ to go from the transmitter to the corner reflector. During that time, the transmitter and receiver have moved a distance Vt_t to position 2. V is the relative velocity between the transmitter-receiver location and the corner reflector. The corner reflector M then retransmits the signal which again takes a time D/c to arrive. Because the original signal came from the transmitter when it was at position 1, it is in that direction that the signal is returned. During the return period, the receiver has moved to position 3 which makes an angle $\beta = 2Vt_t/D = 2V/c$ with the direction in which the corner reflector returned the signal.

As an example, if the retro-reflector were on a satellite with an orbital period of 90 minutes, the relative velocities are sufficient to make B approximately 10 seconds of arc. Unless the beamwidth of the retransmitted energy is at least twice this value, the return will not be detected at the receiver. Assuming that the corner reflector is sufficiently far removed from the transmitter that Fraunhofer diffraction limits hold, the effective aperture of the corner reflector can be no larger than 0.75 centimeters in diameter.

2.4 RANGE CALCULATIONS

A laser transmitter which directs a total power P_T into a beam having a half-power beamwidth of θ_T will illuminate a distant target with an on-axis intensity of

$$I = \frac{\pi}{4} \frac{P_T}{\theta_T^2} \frac{\text{watts}}{\text{steradian}} . \qquad (2.10)$$

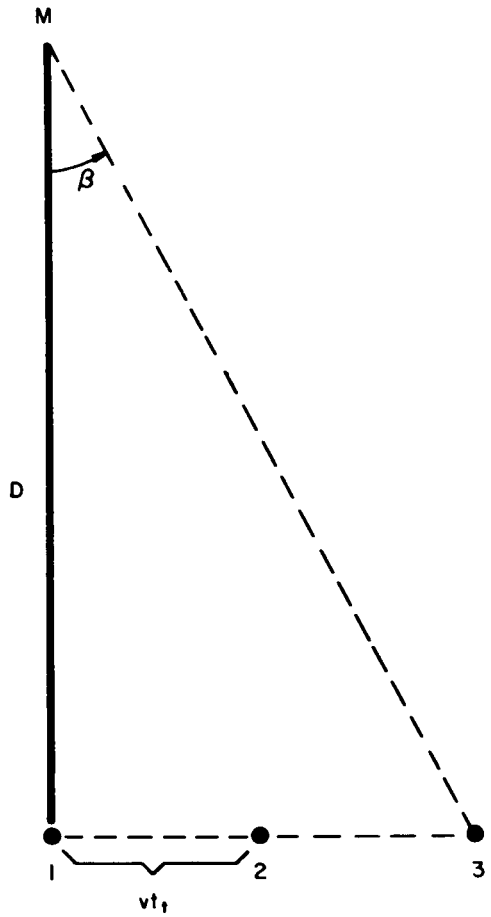

Fig. 2-1. Bradley error for tracking a corner reflector.

An optical corner-reflector of diameter d_c subtends a solid angle of $\pi/4\ (d_c/R)^2$ at a range R. If it were located on the axis of the laser transmitter, it would intercept a total power

$$P_c = \frac{\pi P_T}{4\,\theta_T^{\,2}} \cdot \frac{\pi d_c^{\,2}}{4\,R^2} = \frac{\pi^2 P_T d_c^{\,2}}{16\,\theta_T^2 R^2} \quad . \tag{2.11}$$

The corner reflector redirects the intercepted energy back toward the transmitter. The minimum beamwidth of the return beam is limited by the fact that the reflector divides the beam into six equal sectors, and each of them can have, at best, a diffraction limited beamwidth of

$$\theta_c \approx \frac{\lambda}{d_c} \tag{2.12}$$

where λ is the wavelength of the light and d_s is the "effective diameter" of one of the sectors. This effective diameter, d_s, is determined from the construction in Fig. 2-2 to be

$$d_s \cong \frac{d_c}{3} \tag{2.13}$$

Thus, for this estimate of return beamwidth (Eq. 2.12), the corner reflector is considered to be a collection of six diffraction-limited radiating apertures, each with a diameter equal to one-third the diameter of the corner reflector.

The on-axis intensity of the return beam can now be estimated as

$$I_{return} = \frac{\pi}{4} \frac{P_c}{\theta_c^2} \frac{\text{watts}}{\text{steradian}} \tag{2.14}$$

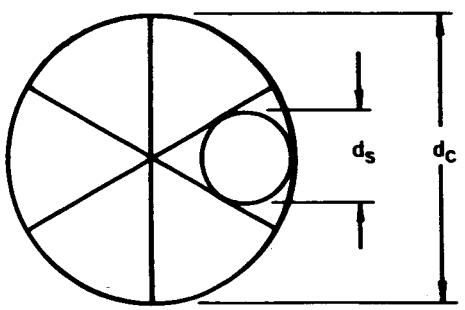

Fig. 2-2. Effective diameter of reflecting sectors of an optical corner reflector.

and the power intercepted by the receiver is

$$P_R = \frac{\pi^2}{16} \frac{P_c d_R^2}{\theta_c^2 R^2} \tag{2.15}$$

After substituting Eqs. (2.11), (2.12), and (2.13) into Eq. (2.15) and including terms for power losses in the transmitter, transmission path, and receiver, the radiant laser power striking the photocathode of the detector is found to be

$$P_R = \left(\frac{\pi}{4}\right)^4 \frac{P_T}{9\lambda^2} \frac{d_c^4 d_R^2}{\theta_T^2 R^4} \left(\frac{1}{L_T L_P L_R}\right) \tag{2.16}$$

Of course, if the receiver aperture is larger than the size of the return beam at the receiver, all of the power which is intercepted by the corner reflector is collected by the receiver, and the received power is

$$P_R = \frac{\pi^2}{16} \frac{P_T d_c^2}{\theta_T^2 R^2} \left(\frac{1}{L_T T_P L_R} \right) \tag{2.17}$$

Equation (2.17) is normally useful when very short ranges are considered, while for long ranges, Eq. (2.16) must be used. In any case, whichever expression results in the lower value of P_R is the correct one on which to base laser requirements.

It is useful at this point to consider a sample calculation for a typical set of parameters. Realistic values for parameters which may be encountered in an optical acquisition and tracking application are:

P_T = 50 milliwatts

d_c = 5 cm ($\sim$ 2 inches)

d_r = 15 cm ($\sim$ 6 inches)

R = 10 kilometers

λ = 6328 Å (He-Ne laser wavelength)

L_T = 3 dB

L_R = 5 dB

L_P = 17 dB (about 2 percent transmission over 20 km)

Using Eq. (2.16) it is found that

$$P_R = \frac{2.76 \times 10^{-9}}{\theta_T^2} \text{ watts } (\theta_T \text{ in minutes of arc}) \tag{2.18}$$

Equation (2.17) gives

$$P_R = \frac{2.88 \times 10^{-8}}{\theta_T^2} \text{ watts } (\theta_T \text{ in minutes of arc}) \tag{2.19}$$

Since the first result Eq. (2.18) is smaller in magnitude than the second, it shows that Eq. (2.16) (and therefore Eq. 2.18) is the correct power equation to use at the 10 km range.

Equation (2.18) is plotted in Fig. 2-3. Also included in the figure are curves representing the received power when the total atmospheric transmittance over the 20 km two-way path is 20 percent (7 dB loss) and 0.2 percent (27 dB loss). These two extremes are attainable under widely variable atmospheric conditions.

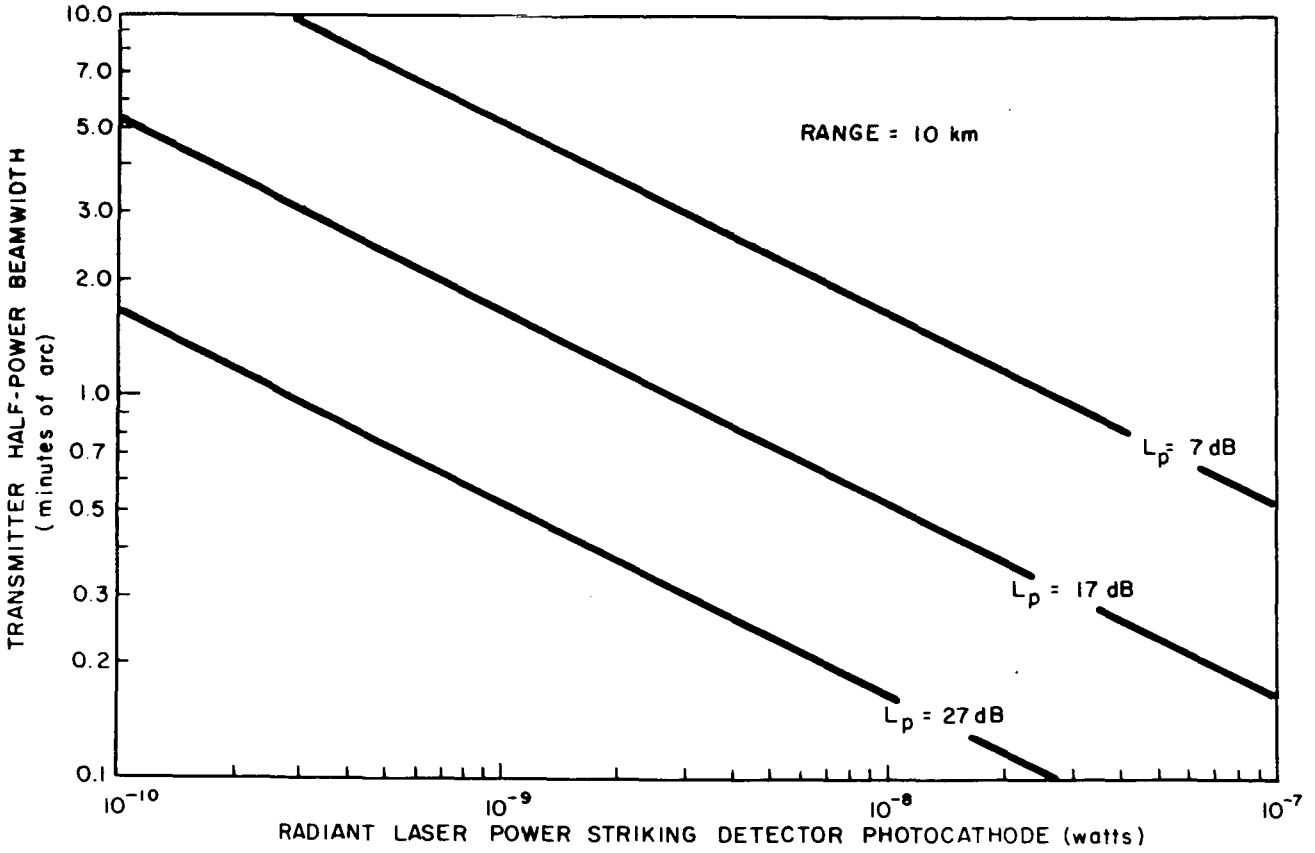

Fig. 2-3. Received laser power versus transmitter beamwidth.

2.5 SIGNAL-TO-NOISE RATIO

In order to determine whether or not the received power is sufficient, the post-detection signal to noise ratio must be evaluated. It will be assumed that the laser output is modulated and that the detector is followed by a narrow band amplifier centered about that modulation frequency. Thus, the ac signal power (in terms of current squared) contained in the cathode photocurrent is

$$\overline{I_S^2} = \frac{m^2}{8} I_o^2 \tag{2.20}$$

where I_o is the dc current which would be produced by the incidence of the peak, unmodulated laser signal, and m is the modulation index. I_o is related to P_R by

$$I_o = \frac{eq}{h\nu} P_R \tag{2.21}$$

where "q" is the quantum efficiency of the photosurface.

If it is further assumed that electron multiplication takes place before discharge into the load, thermal noise in the load resistor can be neglected and the post-detection signal to noise ratio takes the form

$$\frac{S}{N} = 0.8 \frac{\frac{m^2}{8}\left(\frac{eq}{h\nu} P_R\right)^2}{2e\left(\frac{eq}{h\nu}\frac{P_R}{2}\right) B + \left(\frac{eq}{h\nu}\right)^2 (NEP)^2 B + 2e\left(\frac{eq}{h\nu} P_B\right) B}$$

$$\frac{S}{N} = 0.8 \left(\frac{m^2}{8}\right) \frac{qP_R}{2h\nu B} \left[\frac{1}{2} + \frac{q}{2h\nu} \frac{(NEP)^2}{P_R} + \frac{P_B}{P_R}\right]^{-1} \tag{2.22}$$

The first term in the brackets represents quantum noise, equal to 1/2 because the modulation is normally biased about the 1/2 power point. The second term is detector noise, and the third term represents shot noise associated with the background dc light level. The factor of 0.8 in the expression accounts for the S/N degradation in the dynode multiplication.

Using the results of the previous sample calculation and assuming typical values for detector characteristics as listed below, the expected post-detection signal to noise ratio is calculated.

$m = 1.0$ (1000 percent modulation)

$q = 0.06$ (6 percent quantum efficiency for S-20 photocathode)

$B = 30$ kc/s

$NEP = 10^{-16}$ watts/(c/s)$^{1/2}$

$$P_b = 2.2 \times 10^{-10} \theta_R^2 \left(\frac{1}{\frac{1}{2} L_P L_R} \right) \text{watts} \quad (\theta_R \text{ in minutes of arc})$$

$$\frac{S}{N} = \frac{880}{\theta_T^2} \left[0.5 + \left(3.46 \times 10^{-7} \right) \theta_T^2 + \left(10^{-3} \right) \theta_T^2 \theta_R^2 \right]^{-1} \quad (2.23)$$

The assumed background power was calculated from a diffusely reflecting background of reflectance 1.0, illuminated by a sea-level solar irradiance of 1.176 watts/m^2 in a 10 Å bandwidth centered about 6328 Å. The path losses from the target to the receiver are just half the total experienced by the laser beam, and the receiver losses are identical. Therefore, the ratio P_B/P_R is independent of receiver and path losses.

Equation (2.23) is plotted in Fig. 2-4. Also plotted are curves representing performance when the atmospheric transmittance is 20 percent and 0.2 percent as was done in Fig. 2-3.

The bandwidth chosen above was derived by assuming a requirement of successful acquisition at 10 km. The two-way transit time of the light is approximately 70 microseconds. If the transmitter and receiver are scanning together, then the transmitter must dwell on the target for at least twice this time, or 140 μs. Thus, the receiver will see a pulse less than 70 μs in duration and must have a bandwidth greater than $1/70\mu s \simeq 14$ kc/s in order to respond to it. Allowing a factor of two for the target being off axis (therefore being seen for a shorter time during scanning), the minimum required bandwidth is about 30 kc/s.

2.5.1 Required S/N for System Operation

When the laser beam is scanned in search of a corner reflector target, it illuminates the target for only a short time. During this short dwell time (70 μs in the example of the previous section), the receiver must recognize the return signal so that it may stop searching for, and begin tracking the target. Recognition will consist of testing the detector current level with respect to a fixed threshold. If the current rises above the threshold, the receiver will assume it is looking at the target.

Because of constant background noise in the receiver and noise on the incoming signal, however, there is always a probability that the target will be "seen" when it is not there, and missed when it is there. It is the purpose of this section to examine the statistical properties of the noise with reference to these probabilities.

The common approach to noise statistics is to assume that the noise is Gaussian. For Gaussian noise, the noise current is distributed normally, i.e., the probability that the noise current I(t) lies between I and I + dI is

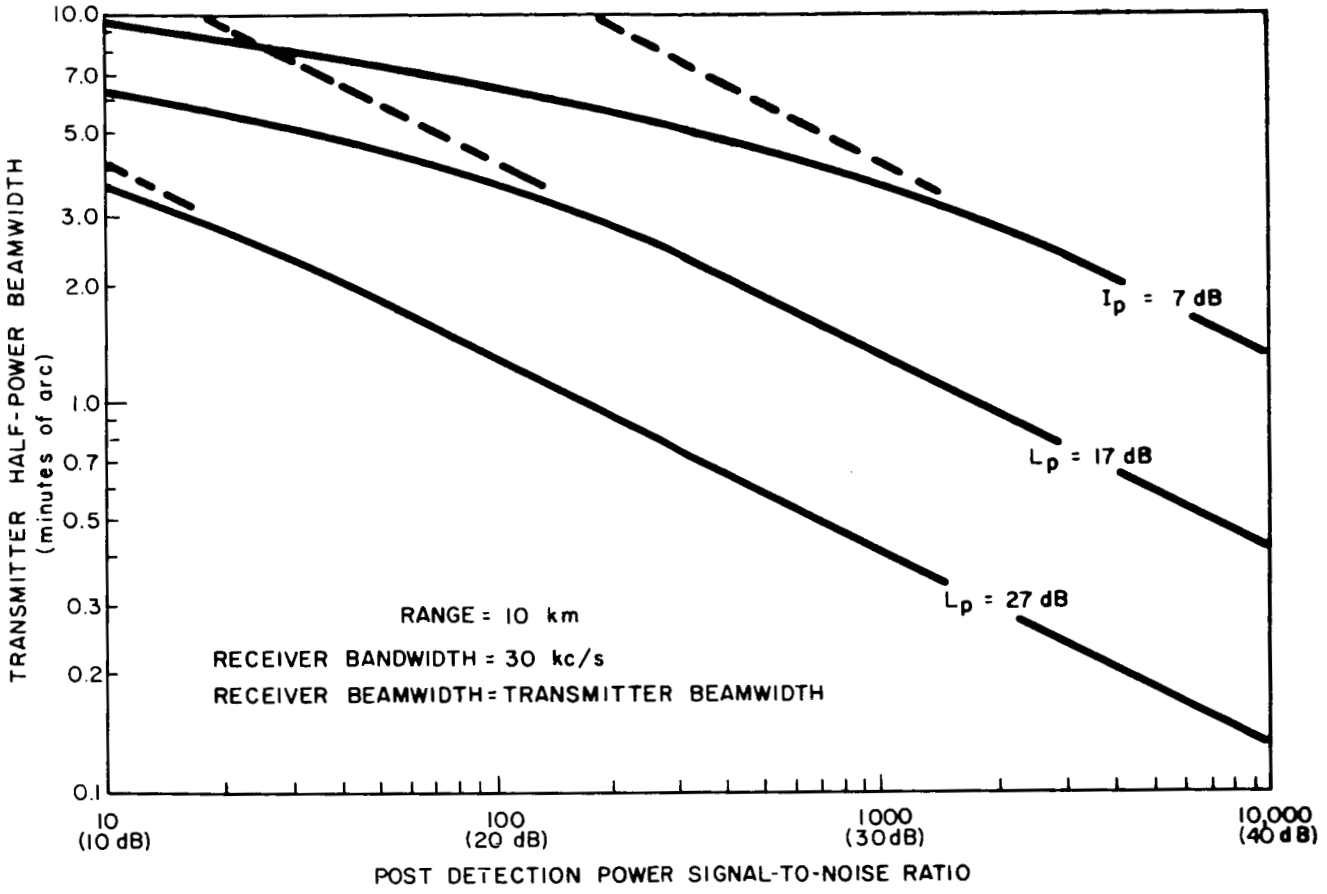

Fig. 2-4. Signal-to-noise ratio versus transmitter beamwidth.

$$p(I)dI = \frac{dI}{\sqrt{2\pi\,\psi_o}} \exp\left(-\frac{I^2}{2\psi_o}\right) , \qquad (2.24)$$

where $\sqrt{\psi_o}$ is the rms value of the noise current. This assumption is correct for most forms of noise encountered in electronic circuits, including thermal noise in resistors and shot noise in vacuum tubes when the average current is sufficiently high. When the average current is small, however, the shot effect current may not be given correctly by a normal distribution law. The variations in current in vacuum tubes are really given by the Poisson distribution, which describes the current in terms of the electrons of which it is comprised. As the average number of electrons per unit time interval becomes large, however, the noise current does approach the normal distribution in Eq. (2.24).

In an optical receiver that uses a photomultiplier, the dominant form of noise is shot noise, or statistical variations in the average current leaving the photocathode. (Thermal noise in the output amplifier is overwhelmed by

the shot noise, because the shot noise is multiplied with the signal approximately one million times in the photomultiplier dynodes.) The current leaving the photocathode consists of photoelectrons produced by light from the background and the target, and electrons produced by thermal emission (the cathode dark current).

To get an idea of how many electrons are involved here, let us make some computations with the figures used in the example of the previous section. With a bandwidth of 30 kc/s, the receiver can detect pulse widths as narrow as 30 μs. In a period of 30 μs, and average of 1/300 dark current electrons and 14 background photoelectrons are emitted (assuming for the background light that θ_R = 1 minute of arc and 1/2 L_P L_R = 19 dB). About 400 signal electrons in the same period are needed to produce a signal-to-noise ratio of 20 dB.

Because of the small number of electrons involved, it is not rigorously correct to use a normal distribution to represent the shot noise current. However, a solution is first obtained assuming that the noise is Gaussian. The predictions of Poisson statistics are then discussed, and data that allow suitable correction factors for the Gaussian curves to be estimated are given. The treatment of the Gaussian noise is taken from the papers by S. O. Rice. [1]

2.5.2 Gaussian Noise Analysis

The output amplifier of the receiver is relatively narrow band, and has a center frequency equal to the expected modulation frequency of the signal. The noise appearing in this amplifier is a sine wave at the center frequency whose amplitude varies in a random fashion with a maximum frequency of approximately one-half the bandwidth. The quantity of interest in describing the noise is the amplitude or the envelope, R(t), of the center-frequency sine wave.

The probability distribution of the noise amplitude, or envelope, is given by the following expression:*

$$P(R)dR = \frac{RdR}{\psi_o} \exp\left(-\frac{R^2}{2\psi_o}\right). \qquad (2.25)$$

The rms value of the noise current is still $\sqrt{\psi_o}$, but the rms value of the envelope is $\sqrt{2\psi_o}$.

1. S. O. Rice, "Mathematical Analysis of Random Noise," Bell System Technical Journal, Vols. 23 and 24.

* Equations (2.25), (2.26), and (2.27) and, with slight modifications, the two curves in Fig. 2-5 were taken directly from reference 1.

Rice goes on to derive several results pertinent to our problem. He studies the distribution of the maxima of R. This is the information we desire because if any particular maxima of the noise current envelope goes above our threshold, an error will result. If the characteristic of the receiver amplifier is that of an ideal band-pass filter with bandwidth B, the following results are obtained:

1. The expected number of maxima per second of the envelope is

$$N = 0.6411\ B. \tag{2.26}$$

2. The probability that a maximum of the envelope selected at random will be greater than $R = y\sqrt{\psi_o}$ is a complicated function which is plotted again y in Fig. 2-5. Following Rice, this probability is denoted $P(R_{max} > y\sqrt{\psi_o})$.

Also plotted in Fig. 2-5 is $P(|I| > y\sqrt{\psi_o})$, which is the probability that the noise current in a low-pass filter will have an absolute magnitude greater than $I = y\sqrt{\psi_o}$.

In all of the curves and equations discussed so far, we have assumed that the noise current is normally distributed. We shall now examine how the predictions of Poisson statistics differ from the results already obtained.

2.5.3 Predictions of Poisson Statistics

Poisson statistics treats the variations in the number of individual electrons leaving the photocathode. For our problem, we are interested in the number of electrons in a time slot of length τ, where τ is related to the receiver bandwidth by $B = 1/2\ \tau$ for a low-pass filter and $B = 1/\tau$ for a band-pass filter.

Let us consider a receiver amplifier with a frequency characteristic in the form of a low-pass filter of bandwidth $B = 1/2\ \tau$. The receiver essentially takes the total number of electrons, n, that arrive in time τ and produces an average current during the interval of

$$I = \frac{e}{\tau} n \tag{2.27}$$

The instantaneous current may be much higher at times during the interval because of the uneven distribution of the electrons, but the limits of the receiver bandwidth prevent the receiver from responding to these shorter-term variations.

Assume the average number of electrons emitted from the photocathode in a time $\tau = 1/2\ B$ is η. Then, the probability that exactly n electrons will be emitted during any period of length τ is given by the Poisson distribution:

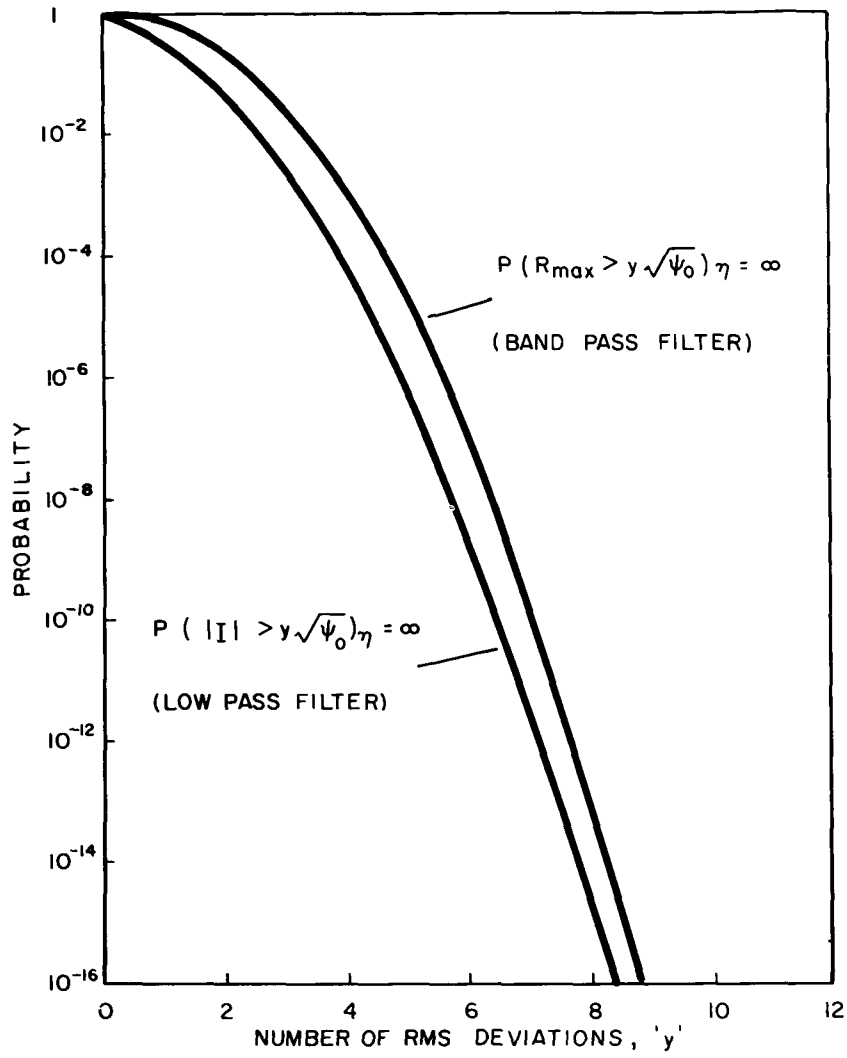

Fig. 2-5. Gaussian noise in low-pass and high-pass filters (after S. O. Rice).

$$p(n) = e^{-\eta} \frac{\eta^n}{n!} \tag{2.28}$$

The mean square deviation from the average value η is given by

$$\overline{\delta^2} = \overline{(n - \eta)^2} = \overline{n^2} - \eta^2 ,$$

or since

$$\overline{n^2} = \sum_{n=o}^{\infty} n^2 P(n) = \eta^2 + \eta ,$$

we have

$$\overline{\delta^2} = \eta. \tag{2.29}$$

The equivalent formulas for the noise current, I_n, can be found by noting that I_n equals the deviation of the actual current from the average current, which from Eq. (2.27) is

$$I_n = I - I_{avg} = \frac{e}{\tau} n - \frac{e}{\tau} \eta \tag{2.30}$$

or

$$I_n = \frac{e}{\tau} \delta .$$

The mean-square noise current is, therefore, from Eq. (2.29)

$$\psi_o = \overline{I_n^2} = \frac{e^2}{\tau^2} \overline{\delta^2} = \frac{e^2}{\tau^2} \eta \tag{2.31}$$

Substitution for $\tau = 1/2B$ and $\eta = (\tau/e)I_{avg}$ brings Eq. (2.31) into the more familiar form:

$$\psi_o = \overline{I_n^2} = 2\, eI_{avg} B \tag{2.32}$$

which is the ordinary shot noise formula.

The distribution of the noise current varies as the average number of electrons changes. Specifically, as the number of electrons decreases, the probability of large deviations from the average current increases. This is shown by the curves in Fig. 2-6 where $P(|\delta| > y\sqrt{\eta})$ is plotted versus y for several

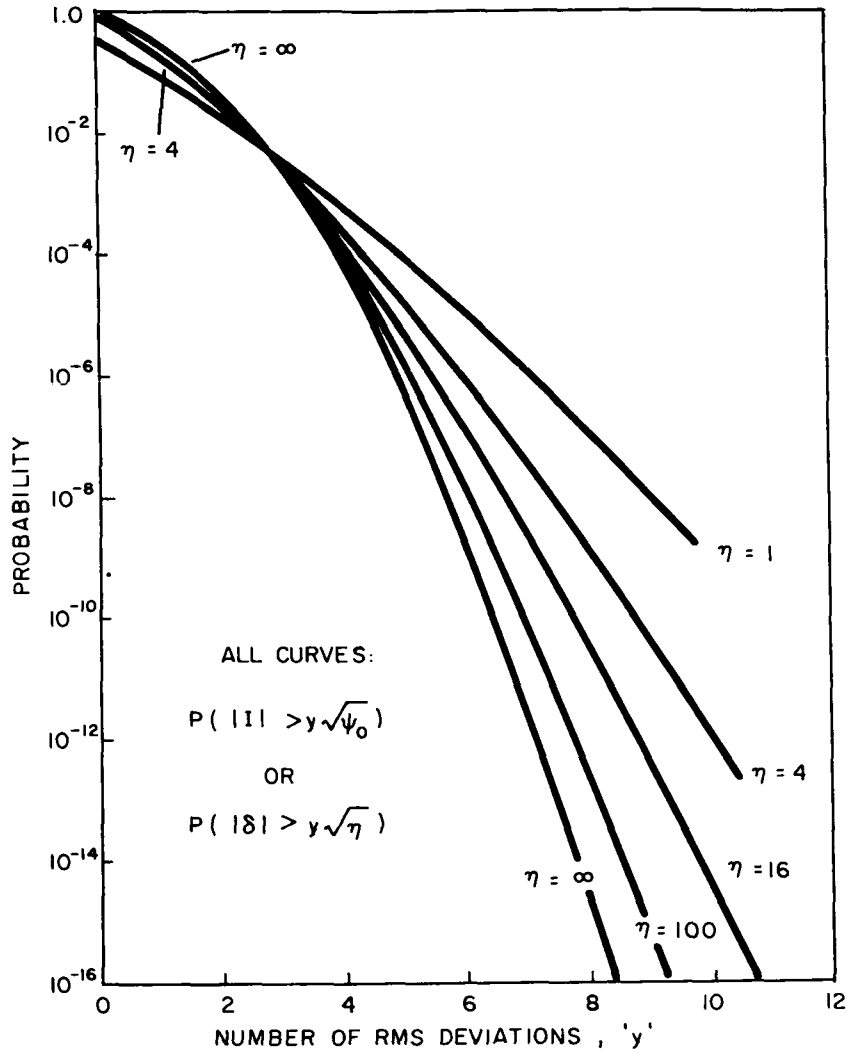

Fig. 2-6. Noise in a low-pass filter.

values of η.* This probability can be written equivalently as $P(|I| > y\sqrt{\psi_o})$ by using Eq. (2.30) and (2.31). However, it must be remembered that I is a discontinuous function and can take on only the discrete values $I = (e/\tau)\delta$ ($\delta = 0, 1, 2, \ldots$). Therefore, the curves for small η are meaningful only when I has one of these values.

---

* $P(|\delta| > y\ \eta)$ is the probability that the number of electrons emitted will differ from the average number by greater than y rms deviations, and is given by the finite sum of probabilities:

$$P(|\delta| > y\sqrt{\eta}) = 1 - \sum_{n=\eta-y\sqrt{\eta}}^{n+y\sqrt{\eta}} p(n)$$

where p(n) is given by Eq. (2.26).

The curve for $\eta = \infty$ represents Gaussian noise, and is identical to the corresponding curve in Fig. 2-5. Both characterize the noise in a low-pass filter. The curves for $\eta = 100$, 16, 4 and 1 in Fig. 2-6 show how the distribution of the noise is distorted from the large current form when the current (number of electrons) becomes small.

We would like to have a similar set of curves for noise in a band-pass filter, or referring to Fig. 2-5, curves of $P(R_{max} > y\sqrt{\psi_o})$ for several small values of η as well as for $\eta = \infty$. However, a solution to this complex problem was not reached.

2.5.4 Interpretation and Application of Results

Since a direct solution of our problem is not available, we must try to estimate the solution from knowledge of the exact solution to a similar problem. Figure 2-5 gives two curves for $\eta = \infty$, and shows the relationship of the band-pass filter curve, $P(R_{max} > y\sqrt{\psi_o})$, to the low-pass filter curve, $P(|I| > y\sqrt{\psi_o})$. Figure 2-6 gives the low-pass filter curves, $P(|I| > y\sqrt{\psi_o})$, for $\eta = \infty$, 100, 16, 4, and 1. If going from $\eta = \infty$ to $\eta = 4$ increases $P(|I| > y\sqrt{\psi_o})$ by some factor, we will assume that going from $\eta = \infty$ to $\eta = 4$ will also increase the curve $P(R_{max} > y\sqrt{\psi_o})$ by the same factor.

The validity of this assumption is not known. It is evident that the probabilities $P(R > y\sqrt{\psi_o})$ and $P(R_{max} > y\sqrt{\psi_o})$ will increase with decreasing η, so that the correction factor is in the right direction. In using this correction procedure, however, one must be aware that what is obtained is only an estimate of the exact solution.

As an example, let us estimate the probability that a maximum of the noise envelope will go above six times the rms noise current level, assuming that the average number of electrons leaving the photocathode in a time $\tau = 1/B$ is 16. From Fig. 2-5, $P(R_{max} > 6\sqrt{\psi_o}) = 10^{-7}$ for $\eta = \infty$. From Fig. 2-6, the ratio of $P(|I| > 6\sqrt{\psi_o})_{\eta = \infty}$ to $P(|I| > 6\sqrt{\psi_o})_{\eta=16}$ is 55. Therefore, our estimate is

$$P(R_{max} > 6\sqrt{\psi_o})_{\eta=16} \approx 55 \times 10^{-7} = 5.5 \times 10^{-6} \qquad (2.33)$$

This procedure was repeated to obtain curves of $P(R_{max} > y\sqrt{\psi_o})$ for $\eta = 1$, 4, 16, 100, and ∞, and these curves are plotted in Fig. 2-7.

If the threshold of the receiver is $y'\sqrt{\psi_o'}$, and the average number of background electrons (from background light and dark current combined) is η_B, i.e., if

$$\psi_o' = 2e\left(\frac{e}{\tau}\eta_B\right)B, \qquad (2.34)$$

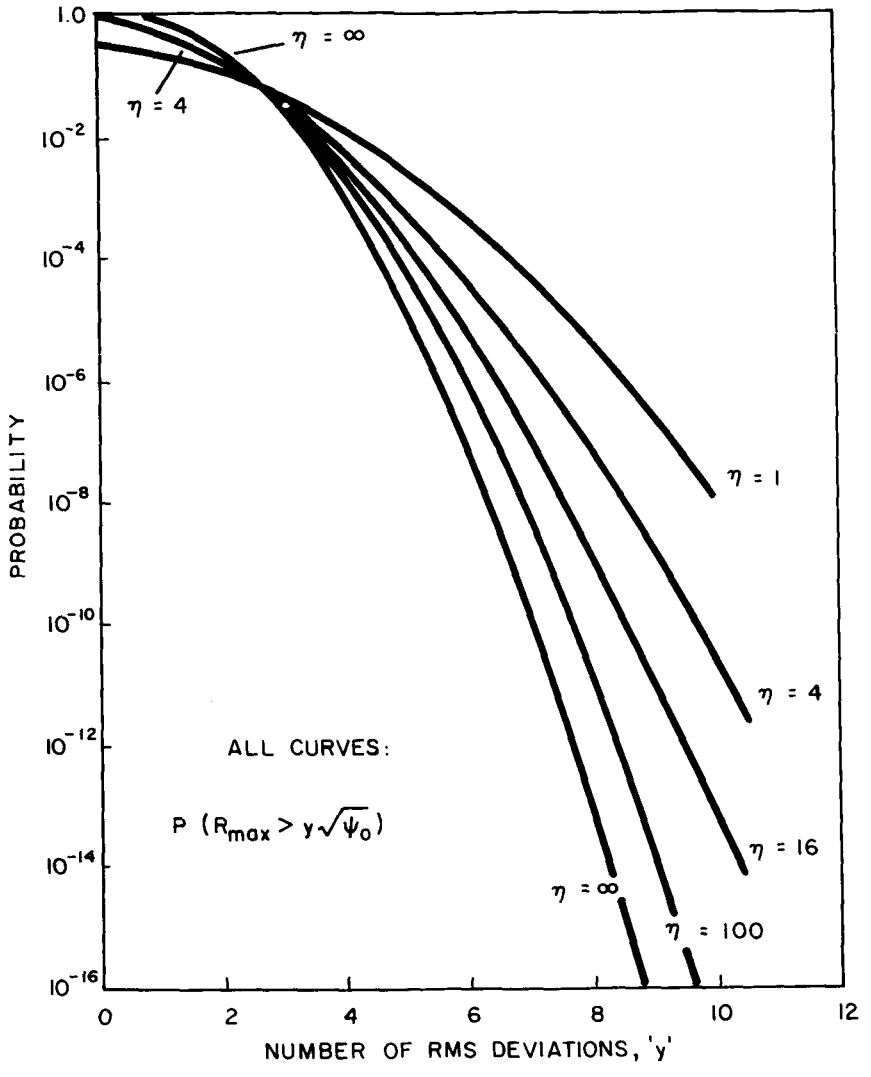

Fig. 2-7. Estimated noise in a band-pass filter.

then the appropriate curve in Fig. 2-7 gives the probability that one of the maxima of the background noise current envelope will be above the threshold. Since, from Eq. (2.26), the number of such maxima occurring each second is 0.6411 B, the average number of maxima per second above threshold is

$$0.6411\ B \left\{ P(R_{max} > y'\sqrt{\psi_o'})_{\eta = \eta_B} \right\} . \qquad (2.35)$$

Multiplying Eq. (2.35) by the acquisition time, T_A, thus gives the average number of false acquisitions per acquisition period, denoted Z'.

It is also necessary to know Z'', the number of times per acquisition period that the signal is missed when it is actually there. When the signal is present,

the average number of electrons is $\eta_s + \eta_B$, and the signal current is, assuming 100 percent modulation,

$$\text{Signal Current} = \frac{e}{\tau}\,\eta_s \cos \omega t. \tag{2.36}$$

The number of times that the envelope of the signal current drops below $(e/\tau)\eta_s - y''\sqrt{\psi_o''}$ is assumed to be approximately one-half the number of times the noise current envelope goes above $y''\sqrt{\psi_o''}$. The quantity ψ_o'' is the mean square noise current when both the signal and the noise are present, or

$$\psi_o'' = 2e\left[\frac{e}{\tau}(\eta_s + \eta_B)\right] B\,. \tag{2.37}$$

The signal is seen only once during the acquisition period, and the time for which it is seen is T_A/N^* where N is the total number of beam positions to be scanned during acquisition. If the signal drops below threshold during this time, the target will be assumed to be missed. The average number of times per acquisition period that the target will be missed is therefore

$$Z'' = 0.6411\, B\left\{\frac{1}{2}\, P(R_{max} > y''\sqrt{\psi_o''}\,)_{\eta=\eta_s+\eta_B}\right\}\frac{T_A}{N} \tag{2.38}$$

The equation for the average number of false acquisition per acquisition period, from Eq. (2.35), is

$$Z' = 0.6411\, B\left\{P(R_{max} > y'\sqrt{\psi_o'}\,)_{\eta=\eta_B}\right\} T_A \tag{2.39}$$

where ψ_o' and ψ_o'' are given by Eqs. (2.34) and (2.37).

For optimum performance, the two error rates Z' and Z'' should be the same when $y'\sqrt{\psi_o'}$ and $(e/\tau)\eta_s - y''\sqrt{\psi_o''}$ correspond to the same amplitude, the threshold amplitude. Thus, the two conditions which must be met simultaneously are

$$Z' = Z'' = \frac{1}{2}\, Z \tag{2.40}$$

---

* This is true only for a raster scan with no overlap. See Section 2.2 for dwell times with other scan modes.

$$R_T = y'\sqrt{\psi_o'} = \frac{e}{\tau}\eta_s - y''\sqrt{\psi_o''} \quad , \tag{2.41}$$

where Z is the total number of errors per acquisition period and R_T is the threshold amplitude. Equation (2.40) yields the requirement that

$$P(R_{max} > y''\sqrt{\psi_o''})_{\eta=\eta_s+\eta_B} = 2N\left\{P(R_{max} > y'\sqrt{\psi_o'})_{\eta=\eta_B}\right\} , \tag{2.42}$$

and Eq. (2.41) implies that

$$y'\sqrt{\frac{\eta_s}{\eta_s}} + y''\sqrt{1 + \frac{\eta_B}{\eta_s}} = \sqrt{\frac{\eta_s}{2}} \quad . \tag{2.43}$$

If specific values are given to the quantities N, η_s, η_B, B, and T_A, a number for Z can be obtained by using the curves in Fig. 2-7 and Eqs. (2.39), (2.42), and (2.43). The method, however, is extremely laborious. The steps taken to find Z are as follows:

1. Substitute η_s and η_B into Eq. (2.43) and put it into the form

$$y' + ay'' = b. \tag{2.44}$$

2. Identify the curves in Fig. 2-7 that correspond to $\eta' = \eta_B$ and $\eta'' = \eta_s + \eta_B$. By trial and error, find values of y' and y'' that satisfy Eq. (2.43) and give probabilities that satisfy Eq. (2.42).

3. Substitute the values for y' and $P(R_{max} > y'\sqrt{\psi_o'})$ found in step 2 into Eq. (2.39) to find Z'.

4. Multiply Z' by 2 and get Z.

Instead of specifying η_s and η_B, the signal-to-noise ratio (SNR) and η_B may be given. The relationships between the two sets of quantities are developed as follows:

The mean square signal current is

$$\overline{(\text{Signal Current})^2} = \frac{1}{2}\frac{e^2}{\tau^2}\eta_s^2 , \tag{2.45}$$

and the mean square noise current is

$$\overline{(\text{Noise Current})^2} = 2\,\frac{e^2}{\tau^2}\,(\eta_s + \eta_B)\,. \tag{2.46}$$

Therefore, the signal-to-noise ratio is

$$\text{SNR} = \frac{\frac{1}{2}\,\frac{e^2}{\tau^2}\,\eta_s^2}{2\,\frac{e^2}{\tau^2}\,(\eta_s + \eta_B)} = \frac{1}{4}\,\frac{\eta_s^2}{\eta_s + \eta_B} \tag{2.47}$$

$$= \frac{1}{4}\,\eta_s\left(\frac{1}{1 + \frac{\eta_B}{\eta_s}}\right)$$

If the SNR and η_B are given, η_s can be found with the formula

$$\eta_s = 2\,\text{SNR}\left[1 + \sqrt{1 + \frac{\eta_B}{\text{SNR}}}\right]. \tag{2.48}$$

Sample curves of the number of errors per acquisition period versus signal-to-noise ratio (Z versus SNR) for several values of constant η_B are plotted in Fig. 2-8. The number of beam positions in the search pattern is assumed to be 100. Actually Z/BT_A is plotted on the ordinate because this quantity is independent of B and T_A. The true error rate can be found by simply multiplying by BT_A.

For an example of the use of the curves in Fig. 2-8, let us consider a system with a no-overlap raster scan acquisition mode. The dwell time on each beam position is T_A/N. Assume that the bandwidth is twice as large as it has to be (as was done in the sample calculations in Section 2.5) so that

$$BT_A = \left(\frac{2}{T_A/N}\right)T_A = 2N\,. \tag{2.49}$$

Thus, the error rate can be found by multiplying the ordinates of the curves in Fig. 2-8 by 200 (since N = 100 for the curves).

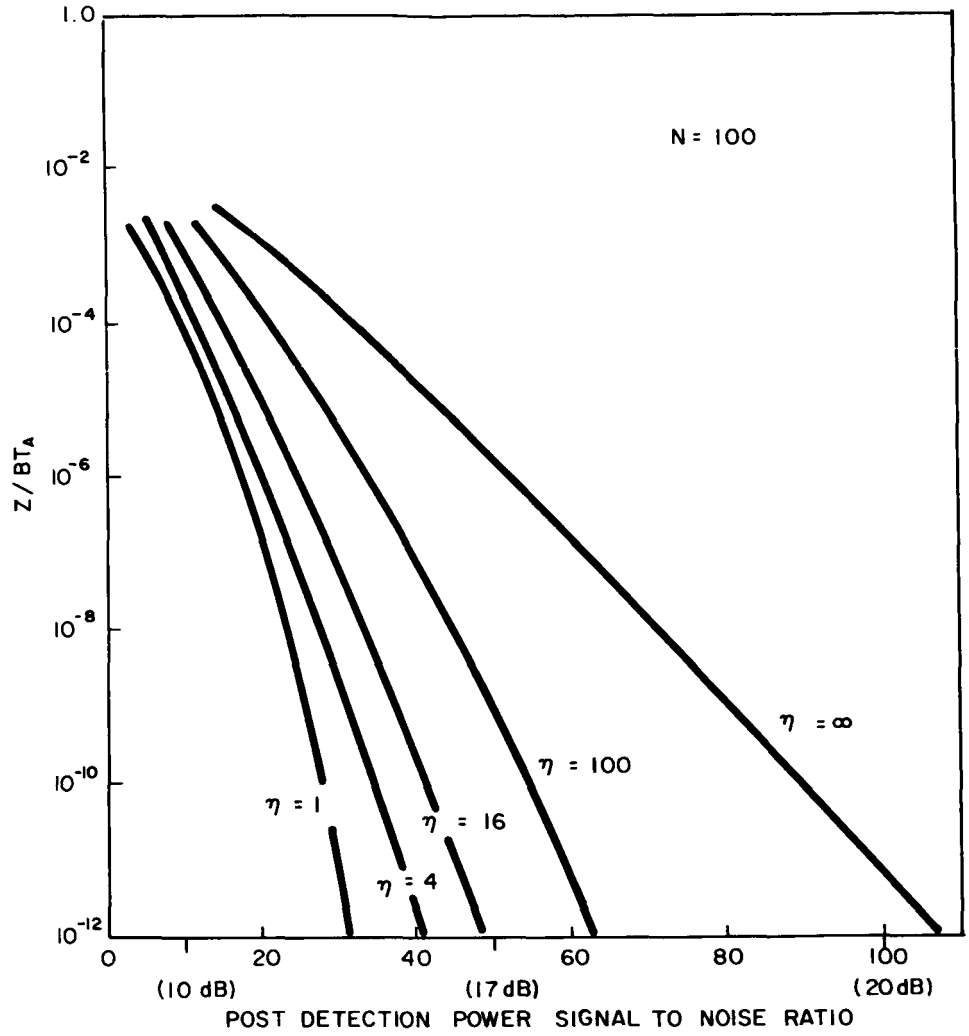

Fig. 2-8. Error rate versus signal to noise ratio.

If the expected background rate amounts to 16 electrons per 1/B time interval, and an error rate of less than one error per 10,000 acquisition periods ($Z = 10^{-4}$) is desired, then the required signal-to-noise ratio is found to be greater than 26, or $\sim$ 14 dB.

The curves in Fig. 2-8 show that as the number of background electrons decreases, the required signal-to-noise ratio for a given error rate also decreases. This seems to contradict the idea that noise would be more bothersome when small numbers of electrons are present. However, one must remember that when the number of background electrons becomes small, the predominant source of noise is the quantum noise in the signal itself. The low background noise allows the threshold to be set low, thus decreasing the probability that when the signal arrives, it will drop below threshold. Indeed, if there are no background electrons, then the optinum threshold is the response caused by one electron. In this case, an error rate of 10^{-4} can be obtained with a signal-to-noise ratio of only 3.5 dB, because the only way an error can occur is if no signal electrons arrive.

Thus, as the ratio of background noise to noise-with-signal decreases, the error rate for a given signal-to-noise ratio will decrease whether the number of electrons involved is large or small. However, if a constant ratio of background to signal noise is maintained, the error rate increases as the number of electrons decreases. The curves in Fig. 2-8 are therefore higher than they would have been if the noise were considered to be Gaussian.

When the curves in Fig. 2-8 are used, it is well to keep in mind the approximations and assumptions made in obtaining them. These are summarized below.

ASSUMPTIONS AND APPROXIMATIONS LEADING TO CURVES IN FIG. 2-8

1. The curves in Fig. 2-7 are only approximations which were obtained by assuming that decreasing the number of electrons increases the noise distribution in a band-pass filter by the same ratio as in a low-pass filter.

2. It is assumed that the receiver output amplifier has the frequency characteristic of an ideal band-pass filter.

3. It is assumed that the threshold is set at its optimum value for each point on the curves.

4. The number of times that the envelope of the signal current drops below threshold is assumed to be one-half the number of times the envelope of the noise current goes above the difference between the threshold level and the average signal level.

5. It is assumed that the lowest error rate occurs when $Z' = Z''$.

6. It is assumed that the signal is modulated 100 percent.

2.6 EFFECTS OF ATMOSPHERE

The use of a narrow laser beam in an optical acquisition system having a fast scan search pattern is complicated by the effects of the atmosphere on the beam. It is known that the beam suffers angular deflections in a random fashion, with peak deflections depending on the path and the condition, but which can exceed 10-20 seconds of arc. It is also known that the beam intensity varies randomly, sometimes falling to less than one-tenth of its average level. The effect of these intensity variations on acquisition was investigated, and the results are summarized below. In particular, the following information was obtained:

1. The probability, $P(I < (1 - \xi) I_o)$, that the signal will be forced below a certain threshold, where the threshold is defined as a fraction $(1 - \xi)$ of the average signal level, I_o.

2. The average length of time, τ_ξ, spent below a threshold $(1 - \xi)I_o$ on a single crossing.

Figure 2-9 shows the appearance of a possible post-detection oscillogram of the return signal when the laser is continuously pointing at the target. The return signal current is given by the equation*

$$I = I_o + I_{noise} \tag{2.50}$$

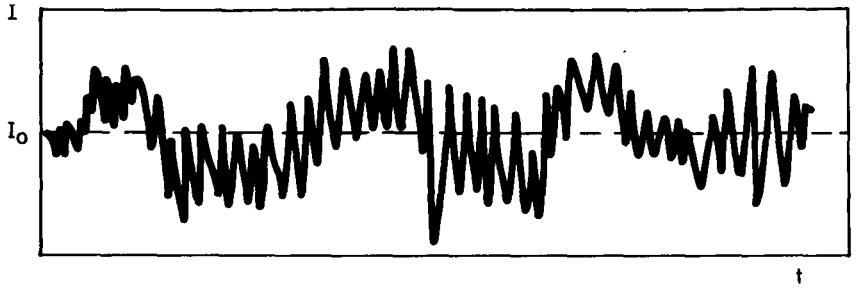

Fig. 2-9. Atmospheric noise on return signal.

If this signal were passed through a perfect, 1-c/s-wide band-pass filter whose center frequency could be varied from 0 - 100 c/s, the rms noise current amplitude could be determined for selected frequencies. If these amplitudes are divided by I_o, a graph of normalized noise amplitude, m(f) versus frequency, f can be drawn, where

$$m(f) = \frac{\text{rms current amplitude in a 1-c/s band around f}}{I_o} \tag{2.51}$$

Statistical information about the noise current can be obtained by representing the sum of the contributions of all frequencies in the form

$$I_{noise}(t) = \sum_{k=1}^{N} \left\{ \sqrt{2\Delta f}\ \ m\ (f_k) \right\} \cos \left[2\pi f_k t - \varphi\ (f_k) \right] , \tag{2.52}$$

where $f_k = k\Delta f$. The phases, $\varphi\ (f_k)$ are assigned randomly and independently to each frequency. The mean-square amplitude of the noise current is found to be

* An identification modulation has a frequency so high as to not be seen on this oscillogram.

$$\overline{I^2_{noise}} = \sum_{k=1}^{N} I_o^2 \, m^2 (f_k) \, \Delta f. \qquad (2.53)$$

Later in the analysis, Δf is allowed to go to zero and N is allowed to go to infinity in such a way that the product $N\Delta f$ remains constant. The mean square noise current then becomes

$$\overline{I^2_{noise}} = \int_o^\infty I_o^2 \, m^2 (f) \, df = \psi_o . \qquad (2.54)$$

Equations (2.52) - (2.54) and the derivation below are based on the work of S. O. Rice.[1] Results obtained in his papers are freely quoted here. When an equation is taken directly from his work, the page number from Vol. 24 of the Bell System Technical Journal is given in parenthesis next to the equation.

Rice chooses to specify the frequency spectrum of the noise in terms of power instead of rms amplitude. Thus, his expressions contain a power spectrum, "w(f)", instead of "m(f)". The two are related by

$$w(f) = m^2(f) \, I_o^2 \qquad (2.55)$$

Using the representation in Eq. (2.52), the mean square noise current is found to be

$$\overline{I^2_{noise}} = \int_o^\infty w(f) \, df = \psi_o = M^2 I_o^2 , \qquad (2.56)$$

(page 47)

where "M" is the normalized rms total noise amplitude.

The probability density function for I_{noise} is

$$p(I) = \frac{1}{2\pi\psi_o} \exp\left(-\frac{I^2}{2\psi_o}\right) = \frac{1}{2\pi} \, \frac{1}{MI_o} \exp\left(-\frac{I^2}{2M^2 I_o^2}\right) . \qquad (2.57)$$

(page 47)

p(I)dI is the probability of finding the current between I and I + dI at any particular time selected at random. This is a normal distribution identical to Eq. (2.24) for high-current shot noise.

The average rate at which noise current crosses zero is given by the expected number of zeros per second:

$$\overline{N_o} = 2\left[\frac{\int_o^\infty f^2\, w(f)df}{\int_o^\infty w(f)dt}\right]^{\frac{1}{2}} \qquad (2.58)$$

(page 54)

The expected number of times per second that the noise current crosses the value "I" with positive slope is given by $\overline{N_{I^+}}$, where

$$\overline{N_{I^+}} = e^{-\frac{I^2}{2\psi_o}}\left[\begin{array}{c}1/2 \text{ the expected number of} \\ \text{zeros per second}\end{array}\right] \qquad (2.59)$$

(page 55)

We will now apply these results to our problem. We have an average dc current I_o, which is a mean value for statistical variations of the type described in Eqs. (2.52) through (2.59). We would like to know the probability of finding the current below some fraction of I_o. Let us define a fraction ξ such that the threshold current* is

$$\text{Threshold Current} = (1 - \xi)I_o \qquad (2.60)$$

Clearly, the probability of finding the total current below $(1 - \xi)I_o$ is one-half the probability that the noise current will exceed ξI_o. The former probability will be denoted $P(I < (1 - \xi)I_o)$, where the capital P suggests a cumulative probability instead of a probability density. From this definition and Eq. (2.57):

$$P(I < (1 - \xi)I_o) = \frac{1}{2}\left(1 - 2\int_o^{\xi I_o} p(I)dI\right)$$

$$= 0.5 - \frac{1}{2}\sqrt{\frac{2}{\pi\psi_o}}\int_o^{\xi I_o} \exp\left(-\frac{I^2}{2\psi_o}\right)dI \qquad (2.61)$$

* This "threshold current" is not related in any way to the threshold levels discussed in Section 2.5.

$$P(I < (1 - \xi)I_o) = 0.5 - 0.5\ \mathrm{erf}\left(\frac{\xi I_o}{\sqrt{2\psi_o}}\right) = 0.5 - 0.5\ \mathrm{erf}\left(\frac{\xi}{2M}\right) \quad (2.62)$$

Up to this point, the form of the frequency spectrum of the noise has not entered into the results. Thus, Eqs. (2.56) through (2.62) are valid for any noise spectrum with a total rms amplitude equal to M. $P(I < (1 - \xi)I_o)$ is plotted in Fig. 2-10 as a function of M for several threshold levels.

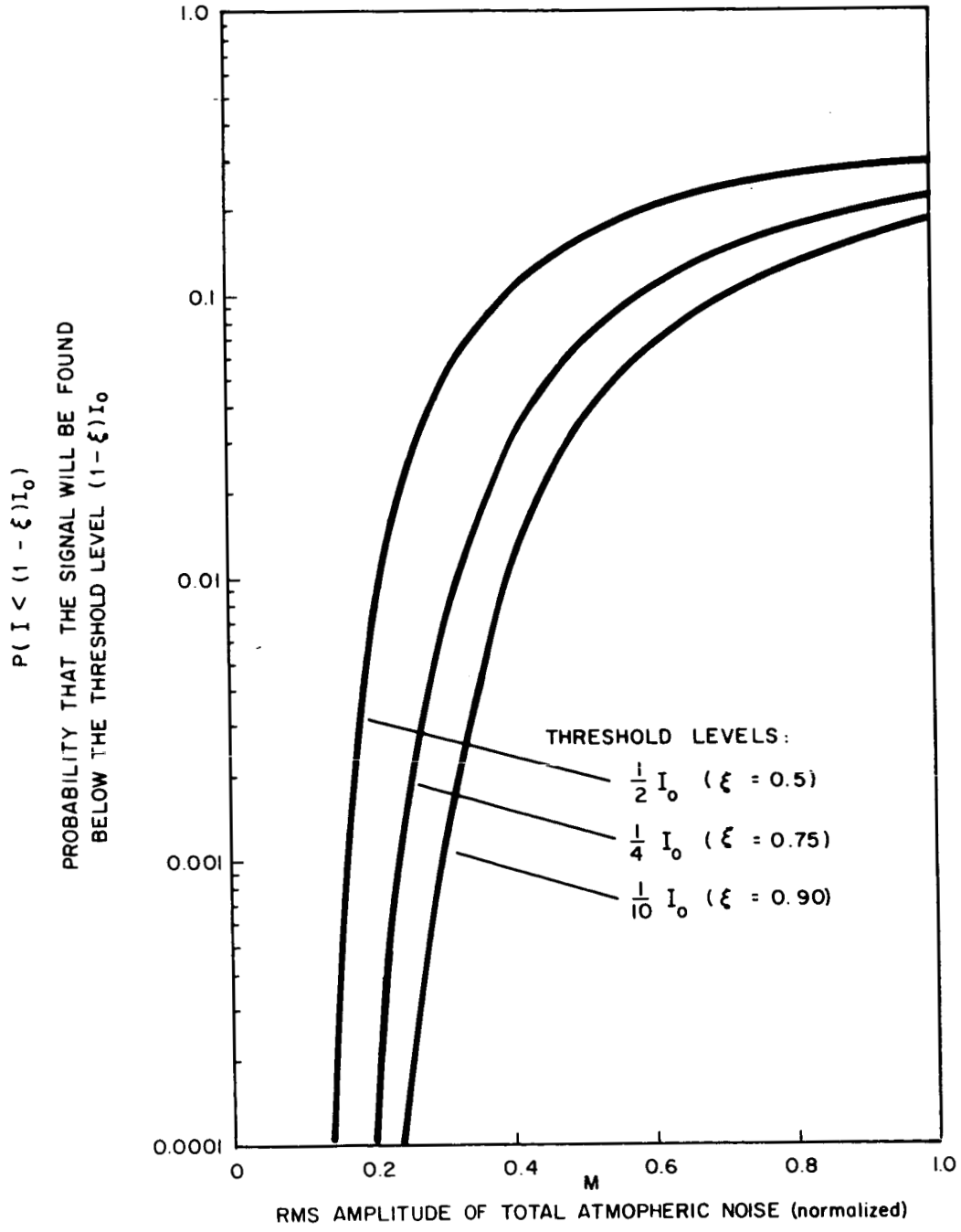

Fig. 2-10. Probability of signal being forced below threshold by atmospheric noise.

To obtain τ_ξ, the average length of time spent below a threshold $(1 - \xi)I_o$ on a single crossing, we note that

$$\tau_\xi = \frac{\text{Average time per second spent below } (1 - \xi)I_o}{\text{Average number of one-way crossings of the level } (1 - \xi)I_o \text{ per second}} \tag{2.63}$$

The numerator of the right hand side of Eq. (2.63) is just $P(I < (1 - \xi)I_o)$ and the denominator is $(1/2)\,\overline{N_{\xi I_o^+}}$. Therefore,

$$\tau_\xi = \frac{P(I < (1 - \xi)I_o)}{(1/2)\,\overline{N_{\xi I_o^+}}}$$

$$= \frac{2}{\overline{N_o}} \left[1 - \operatorname{erf}\left(\frac{\xi}{\sqrt{2M}}\right) \right] \exp\left(\frac{\xi^2}{2M^2}\right) \tag{2.64}$$

The quantity $\overline{N_o}\tau_\xi$ is plotted in Fig. 2-11 as a function of M for several threshold levels.

Numerical estimates of τ_ξ itself cannot be obtained without evaluating $\overline{N_o}$, the expected number of zeros per second.* As shown in Eq. (2.58), $\overline{N_o}$ is dependent on the exact form of the frequency spectrum of the noise, m(f).

Experiments have shown[2,3] that the exact form of this curve is so dependent upon the particular transmission path, atmospheric conditions, transmitter beam size and beamwidth, and receiver size that a "typical" curve is impossible to choose unless a particular system and site are specified. One valid generalization, however, is that most of the noise power is contained in frequencies below 100 c/s. In the range 100 to 1000 c/s, the rms noise amplitude drops off rapidly, and above 1000 c/s it is negligible. These generalizations imply that $\overline{N_o}$ would be on the order of 100 or less. Certainly it should not go above 500 crossings per second.

---

* When I_{noise} crosses zero, I_{signal} crosses the average current, I_o.

2. J. F. Spalding and K. Tomiyasu, "Laser Beam Propagation in the Atmosphere," Proceedings of the First Conference on Laser Technology (Office of Naval Research, Boston 1963). Volume II.

3. R. Paulson, E. Ellis, and N. Ginsburg, "Atmospheric Optical Noise Measurements," Final Report on Contract AF 19(604)-3908, August 15, 1962.

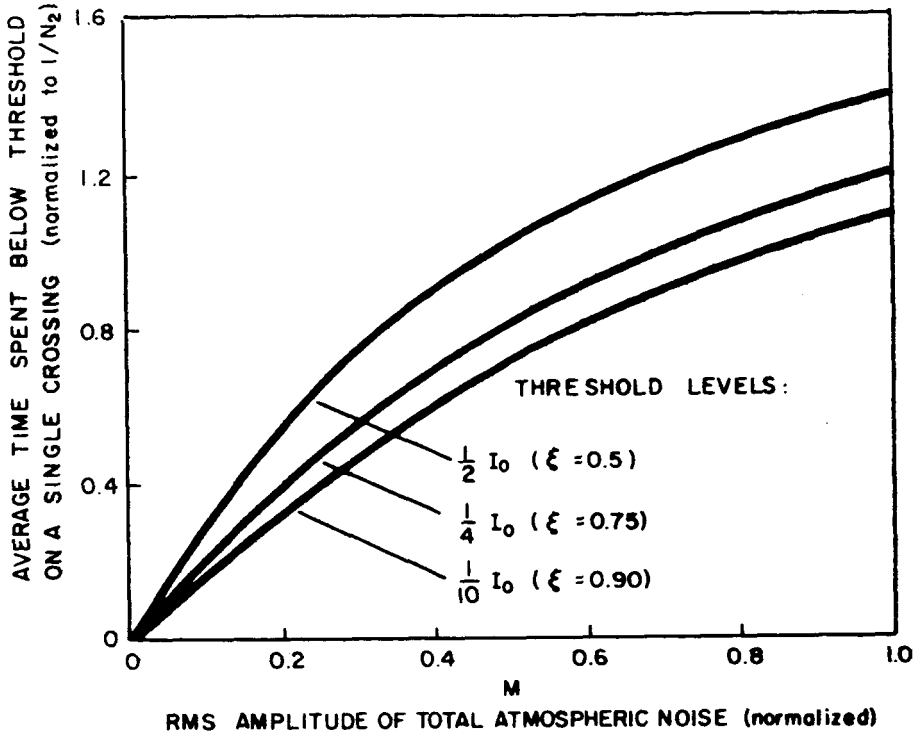

Fig. 2-11. Time spent below threshold on a single crossing.

From Fig. 2-11 the smallest values of $\overline{N}_o\tau_\xi$ that will normally be encountered are around 0.3. When $\overline{N}_o\tau_\xi$ becomes smaller than this, the probability of error (from Fig. 2-10) also becomes negligible. Therefore, using the minimum value of $\overline{N}_o\tau_\xi$ (0.3), and the maximum value of $\overline{N}_o$ (500), the minimum expected value of τ_ξ is

$$\tau_\xi = \frac{0.3}{500} = 600\ \mu s \tag{2.65}$$

This is a worst case analysis; normally τ_ξ will be greater than this, However, it illustrates the point that since the target is only seen for about 70 μs (using numbers from the examples in Section 2.5), the signal will probably be below threshold for the full 70 μs if it is below at the beginning.

The above analysis also shows that atmospheric effects cannot cause the average signal level to change appreciably during a 70 μs period.

2.7 COMBINED EFFECTS OF ATMOSPHERIC AND SHOT NOISE

Because the atmosphere does not change the signal level appreciably during a time of 70 μs, the curves in Fig. 2-10 give the probability that

when the receiver is looking at the target, the average power (number of electrons, η_s) arriving from the target will be below a fraction $(1 - \xi)$ of its mean value. Therefore, if the number of background electrons in the photomultiplier is relatively constant, the curves in Fig. 2-10 also give the probability that the SNR will be below some fraction of its mean value. The SNR is then related to the expected error rate by the curves in Fig. 2-8.

If the SNR is evaluated using I_o, the average signal current, and an error rate, Z, found from Fig. 2-8, then the atmospheric noise will cause the actual error rate to be higher than Z half of the time and lower than Z half of the time. However, the lowest that the error rate could go is (1/2) Z (see Eq. (2.40), whereas it could go much higher than 2Z. Therefore, defining SNR in terms of I_o does not appear to be an optimum choice.

A better choice would probably be to define SNR in terms of (1/2) I_o or (1/4) I_o. This, in effect, introduces a safety factor to assure that the error rate does not go above that given in Fig. 2-8. The optimum magnitude for the safety factor is obviously a function of M.

Further work is necessary on this problem before a true optimization procedure can be outlined. However, the investigation reported here can be used to determine the order of magnitude of error rates. It will also serve as a basis for further efforts.

3. EXPERIMENTAL SYSTEM

A bench test model of a one-dimensional, open-loop laser acquisition and tracking system was built, and one-degree-of-freedom experiments were performed to evaluate developmental beam deflecting devices. A block diagram of the bench test model is given in Fig. 2-12, and photographs of the system are shown in Figs. 2-13 and 2-14. The receiver was originally constructed with a silicon photodiode detector, but because problems in the signal-to-noise ratio developed, it was later modified to use a photomultiplier.

The initial experiments employed an electro-optic refractor of the first kind.[4] Shortly after the program began, however, GT&E Laboratories concentrated their effort on the more promising shear-plate mirror type. Using one of the first shear-plate models, the bench test model was set up and experimental techniques were developed. Precision experiments were then begun with two deflectors, identified as "SPM-4" and "SPM-4B." These experiments continued to the end of the program, and the results of the measurements are summarized in this section under two main headings: "Deflection Characteristics" and "Compensation for Hysteresis."

DC deflection voltages from 0 to $\pm$ 10 kV were supplied by a Del Electronics Model 15-6-1A HV power supply. AC deflection voltages from 0 to 7000 V

4. V. J. Fowler, "Investigation of Electro-Optic Techniques for Controlling the Direction of a Laser Beam," Final Report for Contract NASW-731, August 1964.

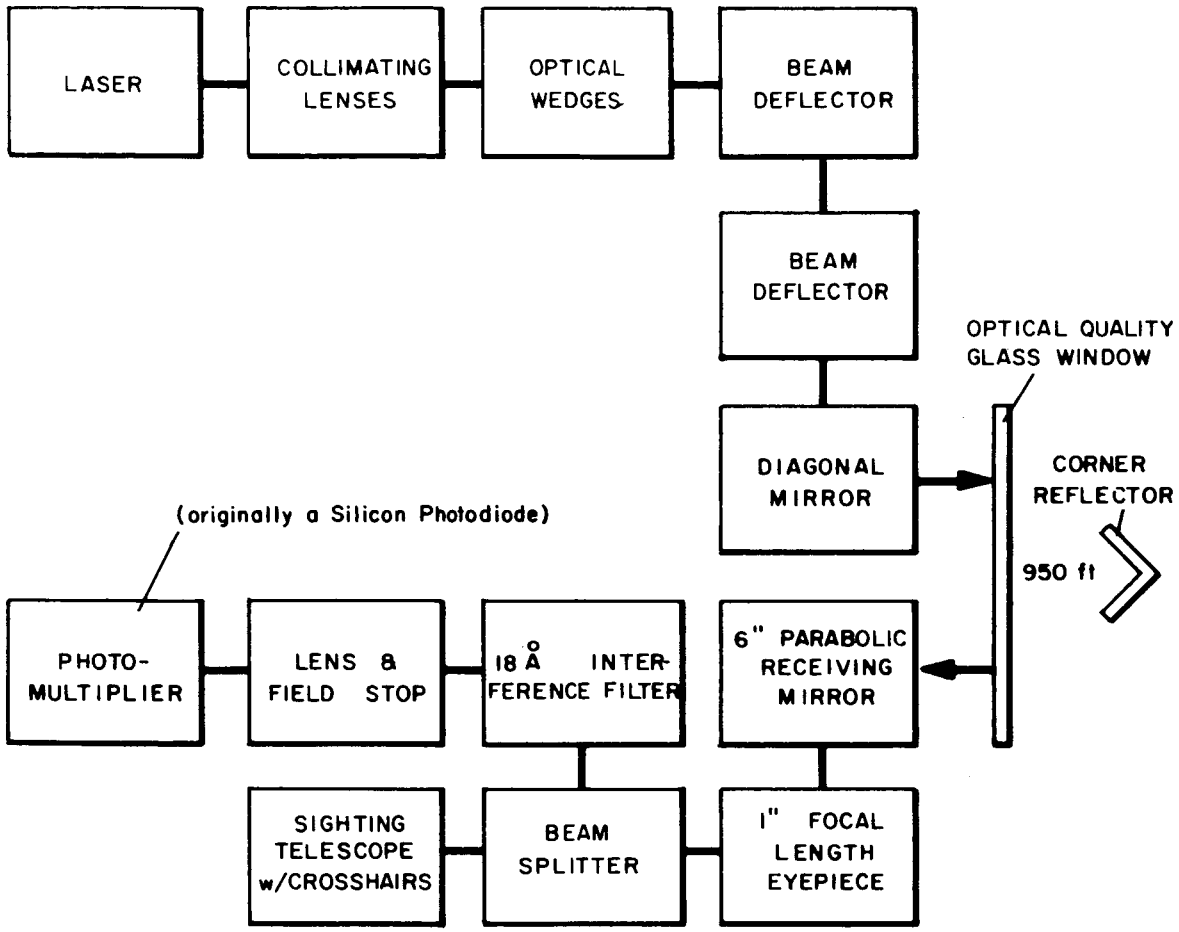

Fig. 2-12. Block diagram of bench test model.

peak to peak were obtained by driving a combination of modulation transformers having a 5 to 1 step-up ratio with a 70-watt audio amplifier. Voltage breakdown in the transformers forced the operation to be limited to 4-5 kV peak-to-peak later in the program, but these voltages were sufficient to perform all of the necessary experiments.

3.1 DEFLECTION CHARACTERISTICS

The deflection characteristics of SPM-4 and SPM-4B were measured using the bench test model and a corner reflector located 950 feet distant. A sinusoidal voltage was applied to one of the deflectors and a signal proportional to this voltage was used to drive the horizontal sweep of an oscilloscope. The return signal from the corner reflector was applied to the vertical input of the oscilloscope. A presentation then appeared which consisted of a horizontal line with a pair of peaks, where hysteresis in the beam

deflector caused two peaks to appear instead of one. The average lateral position of the peaks corresponded roughly to the relative angular position of the corner reflector in the sweep of the laser beam. After calibrating the horizontal scale of the oscilloscope screen, the average voltage representing this angular position could be computed directly.

If the horizontal sweep is driven with a signal directly proportional to the deflection instead of the voltage, only one peak will appear in the oscilloscope presentation instead of two. The apparent angular position in this case is directly proportional to the displacement of the peak.

The corner reflector was mounted on a long board in such a way that it could be moved in the plane of the scanning beam in increments as small as 3/8 inch. At a distance of 950 feet, this increment corresponds to 6.78 seconds of arc. By physically moving the corner reflector a know amount and observing the changing position of the peaks on the oscilloscope screen, the sensitivity of the beam deflectors when driven by an ac voltage was determined.

Once this sensitivity was known, the corner reflector was left stationary and the dc deflection characteristics of one beam deflector were obtained using the ac characteristics of the other as a reference. This was accomplished by arranging the two deflectors in tandem so that they both

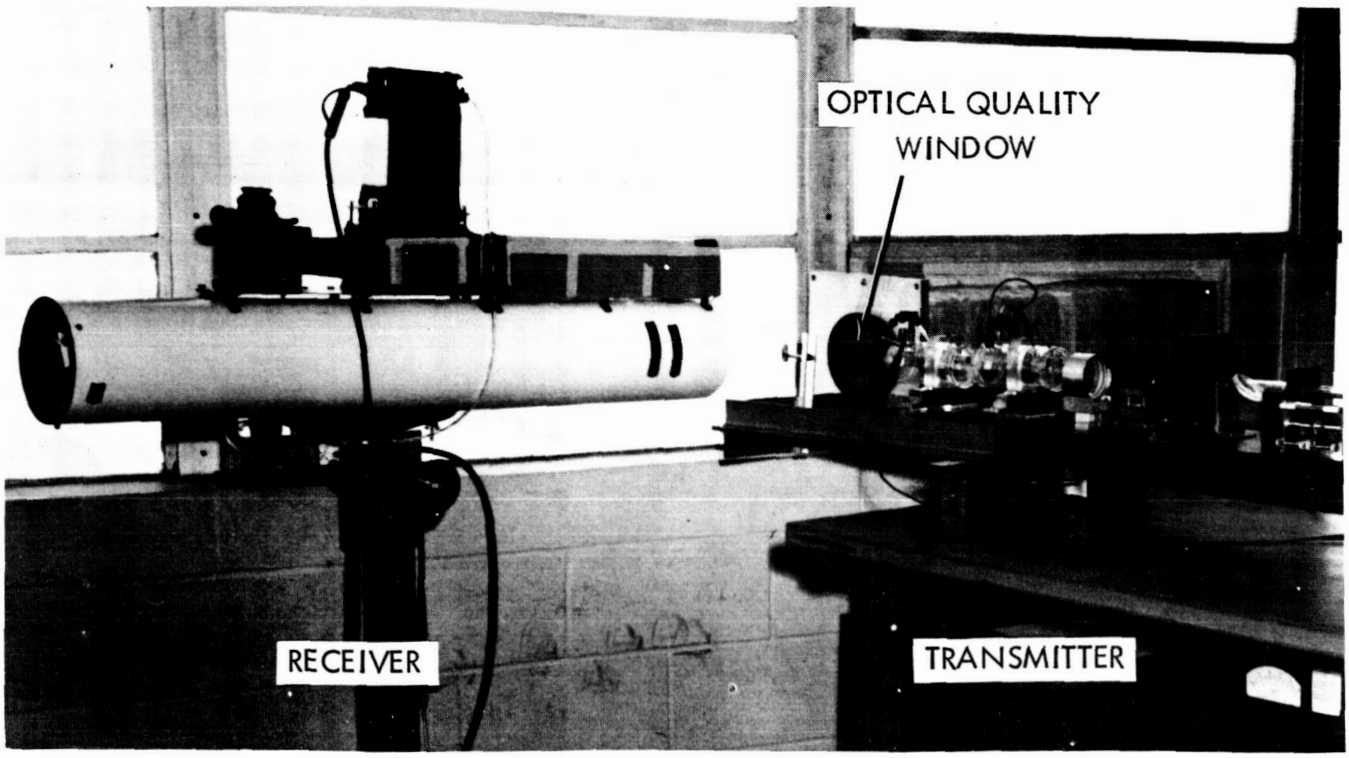

Fig. 2-13. Bench test model of acquisition and tracking system.

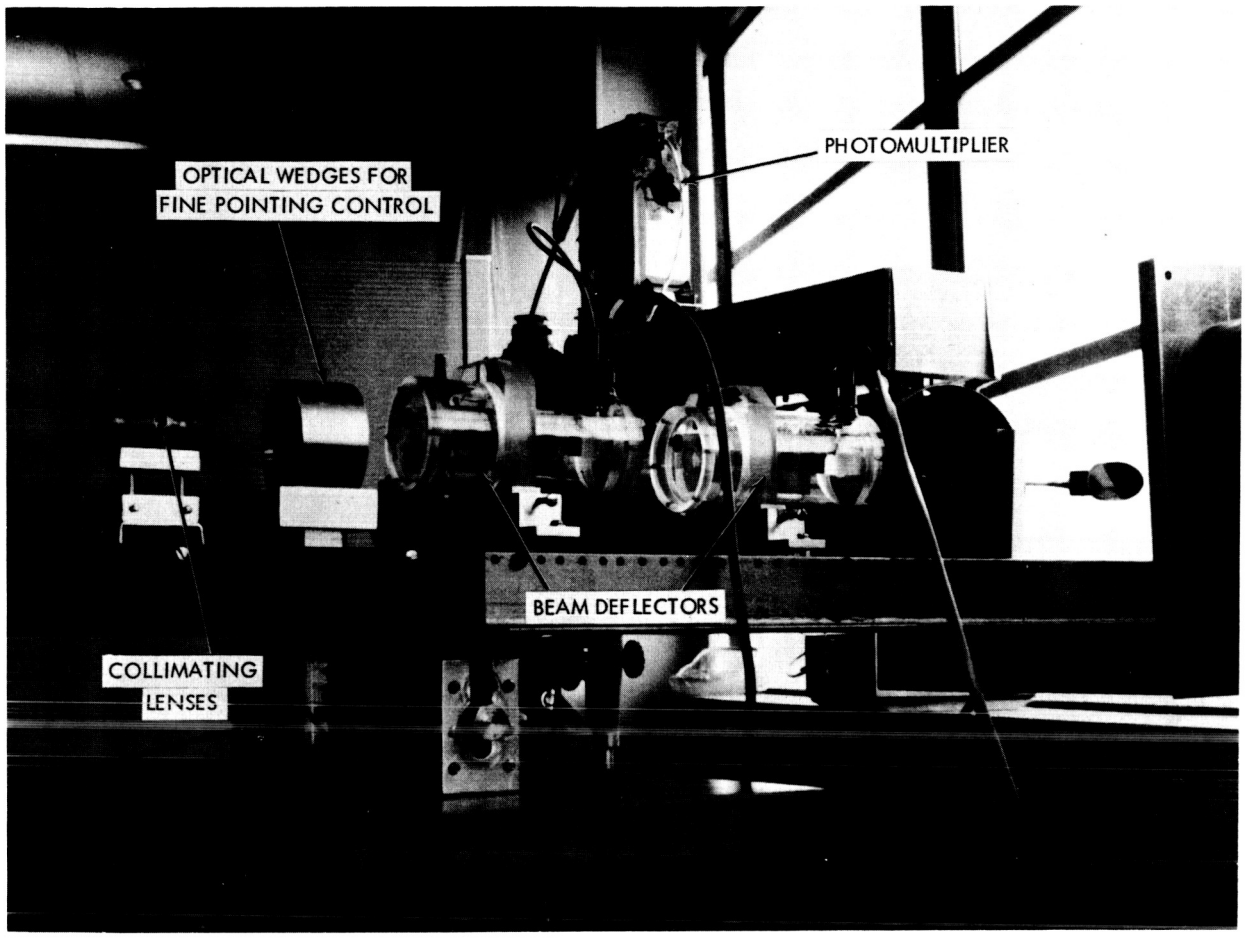

Fig. 2-14. Close-up of transmitter.

deflected the laser beam in the same plane. With an ac voltage on one deflector and zero voltage on the other, an oscilloscope presentation was obtained which had a peak in the center of the sweep. When a dc voltage was applied to the other deflector, it moved the center of the laser beam sweep with respect to the stationary corner reflector. Since this is equivalent to moving the corner reflector with the center of the sweep held stationary, the dc deflection could be computed from the observed displacement of the peak (in volts) and the known ac deflection sensitivity.

3.1.1 DC Deflection Characteristics

The dc deflection characteristics of SPM-4 and SPM-4B cannot be reported in a single graph, because a substantial amount of hysteresis is present in them. Two or more graphs are necessary to describe the behavior: (1) The deflection versus voltage curve of a deflector which had no remanent deflection initially, and (2) One or more hysteresis loops which roughly describe the nature of future deflection as a function of past deflection history, i.e., as a function of the location in the deflection — voltage plane.

Figure 2-15 shows the initial deflection curves of SPM-4 and SPM-4B. The condition of initial zero remanent deflection was met by first subjecting the deflectors to a large amplitude sinusoidal voltage (at a frequency of 1 kc/s) and then decreasing the amplitude slowly to zero. Figure 2-16 gives two hysteresis loops for SPM-4B, representing maximum applied voltages of 2800 and 1000 volts. The hysteresis loops of SPM-4 are similar, and are therefore not shown.

The hysteresis loops demonstrate that, for example, if maximum voltages in the range of ± 3000 volts are used, then at any single voltage, deflections differing by as much as 0.7 minute of arc can be expected. In terms of the minimum attainable beamwidth for the deflectors, this would represent a difference of about two beamwidths.

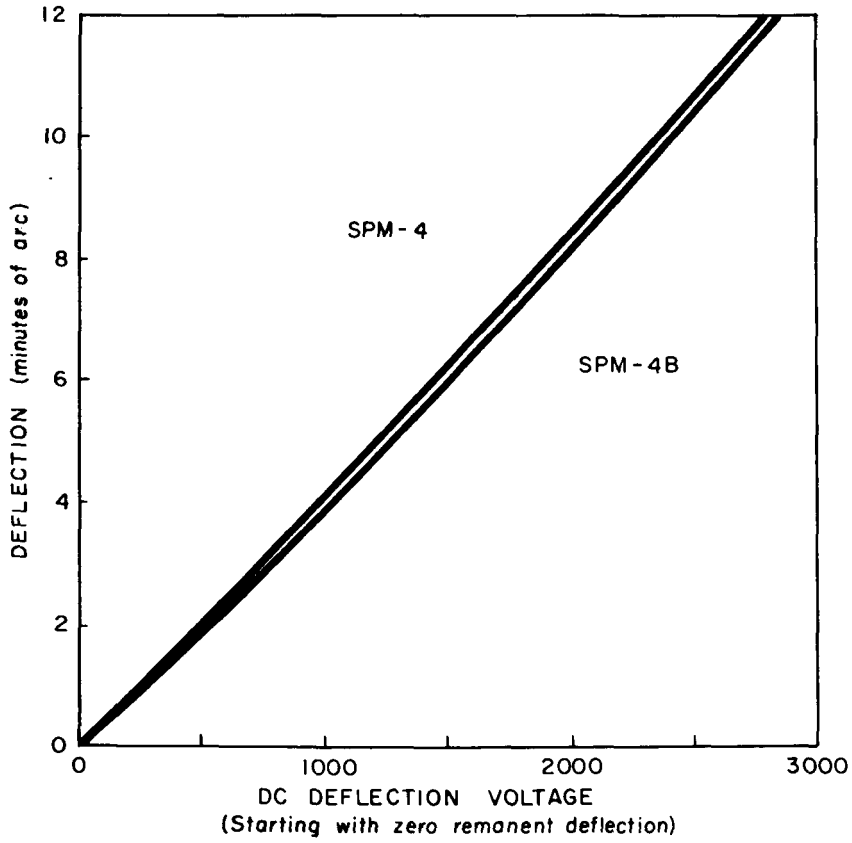

Fig. 2-15. Initial dc deflection curves.

3.1.2 AC Deflection Characteristics

When a beam deflector is driven by a sinusoidal voltage, a plot of deflection versus voltage traces out a hysteresis loop similar to the ones shown in Fig. 2-16. It is for this reason that an oscilloscope display will have two peaks if the horizontal sweep is driven by the beam deflector voltage. Using the calibration constant of the horizontal sweep input, the

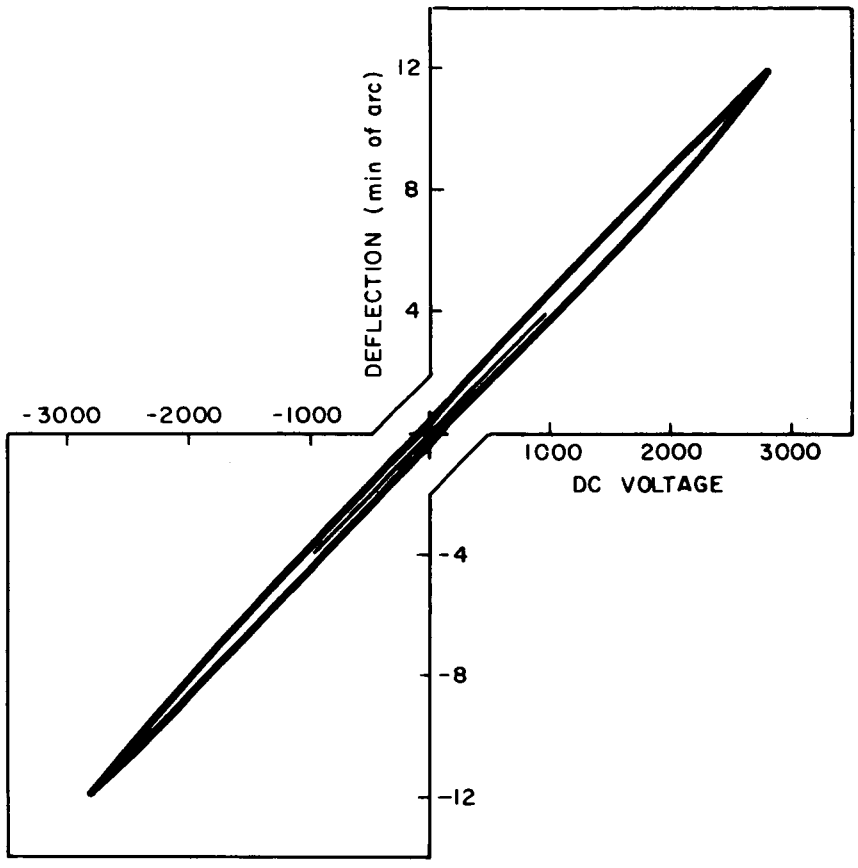

Fig. 2-16. DC hysteresis loops for SPM-4B.

average voltage producing any deflection can be found from the average displacement of the peaks from the center of the sweep.

Single curves of deflection versus this average voltage were obtained for several frequencies and amplitudes in the range 700 to 1600 c/s, and they were found to be virtually identical. A typical example is shown in Fig. 2-17. In the neighborhood of 1700 to 2000 c/s, several structural resonances existed, and these prevented the accumulation of consistent data above 1600 c/s.

Using the same data run represented by Fig. 2-17, a plot of the square of the peak separation versus the square of the angular position is given in Fig. 2-18. The derivation in Appendix A shows that if the hysteresis were really only a pure phase shift, this curve would be a straight line. Thus, the deviation of the actual cruve from the straight line shown indicates the extent of true hysteresis in the ac response of the deflector. It also shows the extent to which the hysteresis can be compensated with a pure phase-shifting network.

If the horizontal sweep is driven by a signal proportional to the deflection (instead of voltage), only one peak appears, and the displacement of that

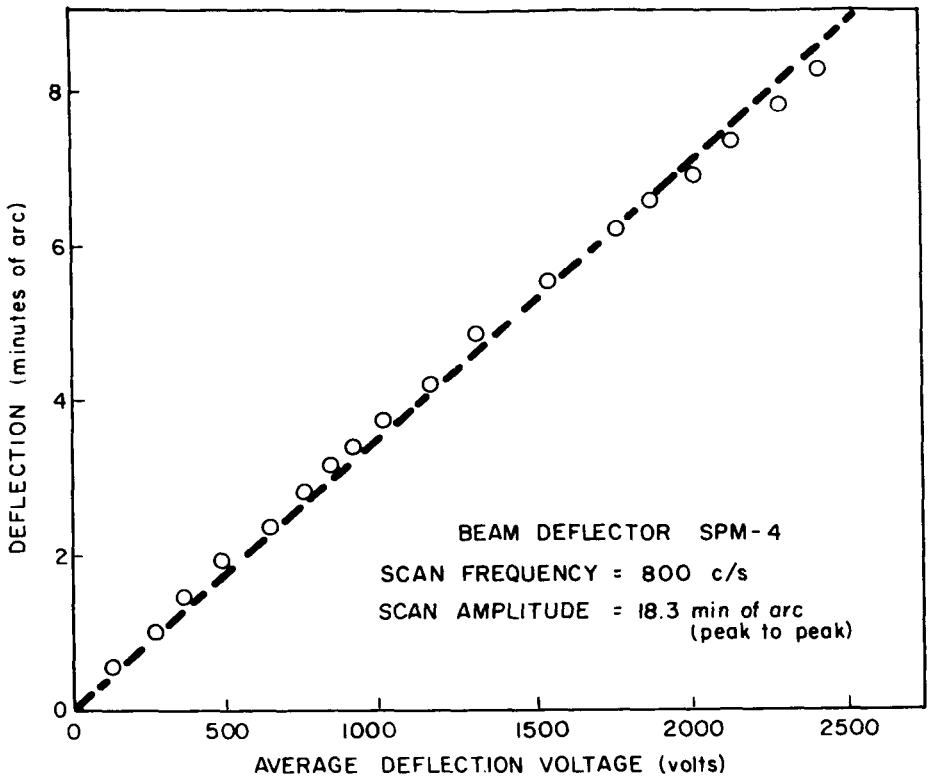

Fig. 2-17. AC deflection characteristics of a shear plate model beam deflector.

peak is directly proportional to the angular position. The ability to derive a signal which is proportional to the deflection is extremely important in acquisition and tracking applications. It was also useful for providing a reference for measuring dc characteristics. Compensation for the hysteresis is discussed further in the following section.

3.2 COMPENSATION FOR HYSTERESIS

The curve in Fig. 2-18 suggests that a simple phase-shifting network is not sufficient to compensate for the hysteresis. (Compensation for hysteresis means causing the two peaks to be coincident at all points across the scan.) This was confirmed by experiments which showed that occasionally a phase shifter could compensate (especially with lower scan amplitudes), but that, in general, the compensation was unsatisfactory. The ability to compensate appeared to be dependent on the purity of the applied sinusoidal waveform, but further experiments with a phase shifter were discontinued when a better approach was found.

The better approach was that of sampling the voltage from across a capacitor in series with the beam deflector. The electrical circuit used is shown in Fig. 2-19. The large resistors in parallel with the beam deflector and

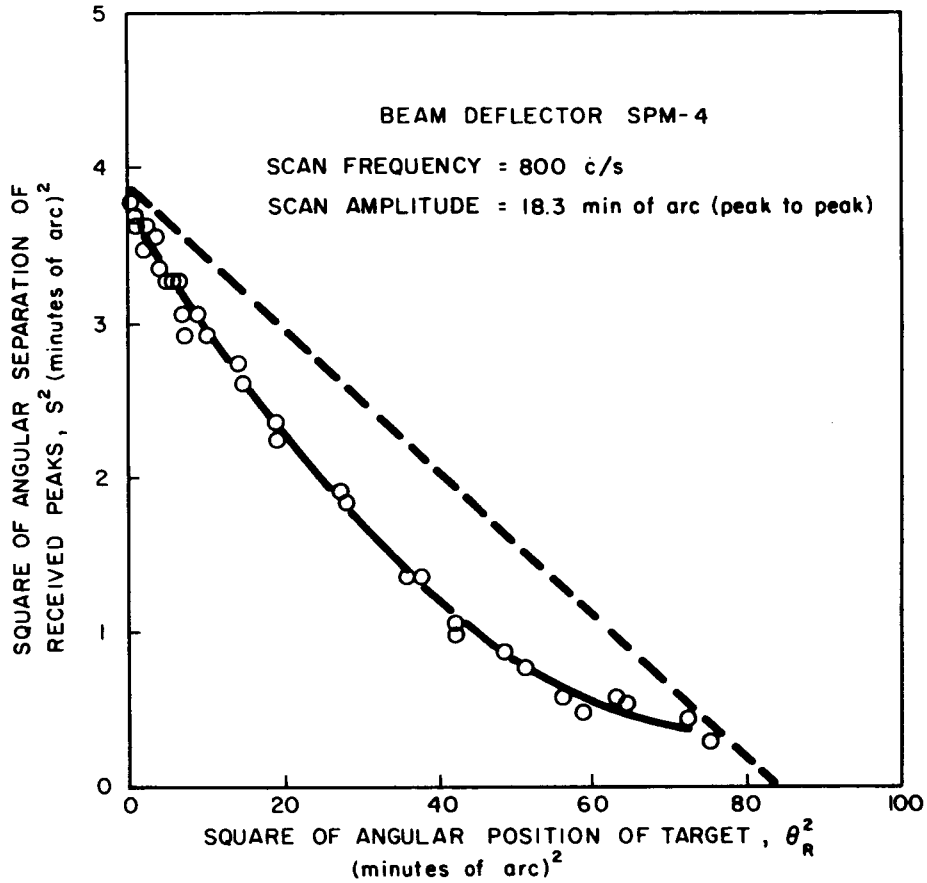

Fig. 2-18. Hysteresis effects in a shear plate model beam deflector.

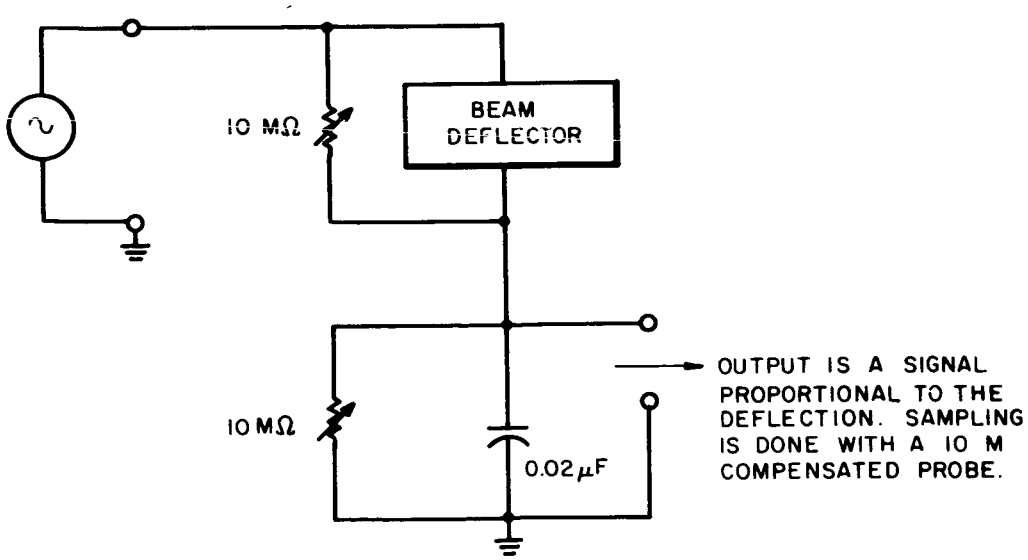

Fig. 2-19. Electrical connections for series-capacitor deflection monitor.

the series capacitor were found to be necessary to cancel out small phase shifts from an undetermined origin. Tests were performed with this method of monitoring the deflection to determine how well it could compensate for hysteresis as a function of the harmonic distortion of the applied waveforms. These tests are described below.

The beam deflector was excited with sinusoidal waveforms of varying amplitude in the frequency range 700 to 2000 c/s. DC voltages on a second beam deflector allowed simulated movement of the corner reflector in the plane of the sinusoidal sweep. Thus, by adjusting this dc voltage, the separation of the peaks in the oscilloscope display could be checked at any position in the sweep. With the horizontal sweep voltage from the series capacitor occupying the entire horizontal scale, separations down to 0.5 percent of the peak to peak deflection could be measured.

The harmonic contents of waveforms which allowed compensation to better than 0.5 percent across the entire sweep were measured at frequencies across the range noted above. Similarly, the content of waveforms for which compensation could not be accomplished was measured. These measurements consisted of determining the relative amplitude of the first nine harmonics with a General Radio low-frequency wave analyzer. The relative power in a given harmonic is obtained by squaring the relative amplitude, and the total power in all the harmonics is obtained by adding the relative powers of each. Unless otherwise stated, the relative power will be used for discussion, even though the amplitude was actually measured.

The ability of the series capacitor monitor to compensate for hysteresis was found to be a function of harmonic distortion only in general sense, i.e., if the waveform becomes grossly distorted, compensation is not possible; if the waveform has low harmonic distortion, compensation is usually possible.

However, the condition of low harmonic distortion is not sufficient to assure that compensation can be accomplished. Resonances in the beam deflector structure were found to be more important in determining the ability to compensate. Quantitative results leading to the above conclusions are discussed below.

For waveforms with peak-to-peak amplitudes of 0 to 8000 volts and with 0.1-0.2 percent total power in the harmonics, compensation to better than 0.5 percent across the entire sweep was found to be possible throughout most of the 0.7 to 2 kc/s frequency range. When the total power in the harmonics was increased to 1 to 2 percent, the peaks in the oscilloscope display were generally separated at the ends of the sweep by about 2 to 3 percent of the peak-to-peak scan amplitude. In contrast to this general behavior, the data taken at two nearby frequencies, 1380 and 1400 c/s, illustrate the large effect of structure resonances. Both waveforms had peak-to-peak amplitudes of about 8000 volts, and both had a total harmonic power content of 0.15 percent. However, compensation was successful at 1400 c/s to about 0.5 percent, whereas at 1380 c/s, the peaks were separated by 4 percent of the peak-to-peak scan amplitude; i.e., at the center

of the sweep the peaks coincided, but at the ends, they were separated by 0.04 x 8000 = 320 volts. This behavior is evidently caused by a structural resonance at 1380 c/s.

Similar behavior was noted in the neighborhood of several structural resonances between 1800 and 2000 c/s.

Thus, if structural resonances are avoided, the series capacitor monitor can compensate for beam deflector hysteresis as described above, provided that the total power in the harmonics is less than 0.1 to 0.2 percent of that in the fundamental. This is not a very stringent requirement for waveform purity, as a wave having second and third harmonics with relative amplitudes of 2.5 percent would easily be satisfactory.

APPENDIX A

To analyze the effect of a pure phase delay between the voltage applied to a beam deflector and the observed angular deflection, let us consider that the applied voltage has the form

$$V = V_o \cos \omega t. \tag{A-1}$$

If the deflection is also sinusoidal with a phase delay of $\omega\tau$, the angular deflection is given by

$$\theta = \theta_o \cos \omega(t - \tau), \tag{A-2}$$

where

$$\frac{\theta_o}{V_o} = K \text{ (radians/volt)} \tag{A-3}$$

Suppose the corner reflector is located in the plane of the scan and at an angle θ_R from the center of the scan. Then, when $\theta = \theta_R$, a signal is received and a peak appears on the oscilloscope display. The beam crosses the reflector two times in each cycle, at times t_1 and t_2.

$$\theta_R = \theta_o \sin \omega(t_1 - \tau) = \theta_o \sin \omega(t_2 - \tau) \tag{A-4}$$

At these two times, the beam deflector voltages (horizontal displacement on the oscilloscope screen) are

$$V_{t_1} = V_o \sin \omega t_1, \quad V_{t_2} = V_o \sin \omega t_2 \tag{A-5}$$

The angular position of the corner reflector is measured from the oscilloscope display by finding the average displacement of the two peaks in volts and multiplying by K from Eq. (A-3),

$$(\theta_R)_{\text{measured}} = K\left(\frac{V_{t_1} + V_{t_2}}{2}\right) = \frac{\theta_o}{2} (\sin \omega t_1 + \sin \omega t_2) \tag{A-6}$$

and the angular separation of the peaks is

$$S = K(V_{t_1} - V_{t_2}) = \theta_o (\sin \omega t_1 - \sin \omega t_2) . \qquad (A-7)$$

The quantities S and $(\theta_R)_{measured}$ can be expressed in terms of the phase delay, $\omega\tau$.

Equation (A-4) implies that the following two equations hold:

$$\omega (t_1 - \tau) = \frac{\pi}{2} - \varphi \qquad (A-8)$$

$$\omega (t_2 - \tau) = \frac{\pi}{2} + \varphi. \qquad (A-9)$$

Subtracting (A-8) from (A-9) and dividing by two gives

$$\varphi = \frac{\omega}{2}(t_2 - t_1).$$

Thus, Eq. (A-4) becomes

$$\theta_R = \theta_o \sin \omega(t_1 - \tau) = \theta_o \sin (\tfrac{\pi}{2} - \varphi) = \theta_o \cos \varphi$$

$$\theta_R = \theta_o \cos \frac{\omega}{2}(t_2 - t_1). \qquad (A-10)$$

If Eqs. (A-8) and (A-9) are added, we find that

$$\omega(t_1 + t_2) - 2\omega\tau = \pi$$

or

$$\frac{\omega}{2}(t_1 + t_2) = \frac{\pi}{2} + \omega\tau. \qquad (A-11)$$

Using trigonometric identities, Eqs. (A-6) and (A-7) can be written

$$(\theta_R)_{measured} = \frac{\theta_o}{2} \sin \omega t_1 + \sin \omega t_2 =$$

$$\theta_o \sin \frac{\omega}{2}(t_1 + t_2) \cos \frac{\omega}{2}(t_1 - t_2), \qquad (A-12)$$

and

$$S = \theta_o (\sin \omega t_1 - \sin \omega t_2) =$$

$$\theta_o \sin \frac{\omega}{2}(t_1 - t_2) \cos \frac{\omega}{2}(t_1 + t_2) \qquad \text{(A-13)}$$

But by using Eqs. (A-10) and (A-11), it is seen that

$$\cos \frac{\omega}{2}(t_1 - t_2) = \frac{\theta_R}{\theta_o}$$

$$\sin \frac{\omega}{2}(t_1 - t_2) = \left(1 - \frac{\theta_R^2}{\theta_o^2}\right)^{\frac{1}{2}}$$

$$\sin \frac{\omega}{2}(t_1 + t_2) = \sin \left(\frac{\pi}{2} + \omega\tau\right) = \cos \omega\tau$$

$$\cos \frac{\omega}{2}(t_1 + t_2) = \cos \left(\frac{\pi}{2} + \omega\tau\right) = -\sin \omega\tau$$

Thus, Eqs. (A-12) and (A-13) can be reduced to

$$(\theta_R)_{\text{measured}} = \theta_R \cos \omega\tau \qquad \text{(A-14)}$$

$$S = 2 \sin \omega\tau \left(\theta_o^2 - \theta_R^2\right)^{\frac{1}{2}}, \qquad \text{(A-15)}$$

or

$$S^2 = (4 \theta_o^2 \sin^2 \omega\tau) - (4 \sin^2 \omega\tau)\, \theta_R^2 . \qquad \text{(A-16)}$$

Equation (A-14) shows that the double peaks caused by a phase delay in the beam deflector response can result in errors in the measurement of angular position.

Equation (A-16) predicts that, for a pure phase shift, the square of the separation of the peaks is a linear function of the square of the angular position of the target. Furthermore, a straight line graph of S^2 versus θ_R^2 must intercept the θ_R^2 axis at $\theta_R^2 = \theta_o^2$. The slope of the graph is a continuously variable function of the phase delay.

In summary, a graph of S^2 versus θ_R^2 will have the following characteristics:

X-intercept = θ_o^2

slope = $-4 \sin^2 \omega\tau$.